Millimeter Wave Electron Spin Resonance Using Quasioptical Techniques

KEITH A. EARLE, DAVID E. BUDIL,[1]
AND JACK H. FREED

BAKER LABORATORY OF CHEMISTRY
CORNELL UNIVERSITY
ITHACA, NEW YORK 14853

I. Introduction

We describe the design principles of electron spin resonance (ESR) spectrometers operating at millimeter wave frequencies that use quasioptics to propagate the excitation radiation instead of conventional waveguide techniques. The necessary background for understanding the operation and limitations of the quasioptical components, which guide the Gaussian beam, as well as a thorough discussion of the design criteria is presented. The quasioptical formalism developed here is used to evaluate the performance of a novel reflection mode spectrometer.

Electron spin resonance (ESR) is a well-established experimental method that has conventionally been limited to 35 GHz and lower in frequency. During the course of the last decade, workers in a number of laboratories (Grinberg *et al.*, 1983; Haindl *et al.*, 1985; Lynch, *et al.*, 1988; Barra *et al.*, 1990; Wang *et al.*, 1994) developed instruments that have pushed the maximum observation frequency up to nearly 1 THz (1000 GHz). Pulse methods at frequencies up to 604 GHz also have been developed (Weber *et al.*, 1989; Bresgunov *et al.*, 1991; Prisner *et al.*, 1992; Moll, 1994), as well as Electron Nuclear Double Resonance (ENDOR) (Burghaus *et al.*, 1988).

The motivation for this intense activity is the resolution enhancement available from higher Larmor fields, which enables small *g*-tensor splittings to be readily observed (Earle *et al.*, 1994). For systems with large zero field splittings (Lynch *et al.*, 1993), high-field spectra can be much simpler to analyze than *X*-band spectra, which increases the reliability and eases the interpretation of the data. In the study of fluid media (Earle *et al.*, 1993), the increased importance of the *g*-tensor contributions vis-à-vis the hyperfine tensor contributions (e.g., for nitroxide spin labels) gives information that is complementary to lower-field studies. These concepts are discussed more fully elsewhere (Lebedev, 1990; Budil *et al.*, 1989), and we refer the reader to the references for a more complete discussion.

The number of laboratories that are exploring the possibilities of high-field ESR is increasing. For spectrometers up to 150 GHz in frequency, microwave techniques have been dominant and may, in fact, be the optimum choice for those frequencies. In a conventional ESR spectrometer, waveguide technology is used to connect the cavity, the source, and the detector. At *X*-band, say, this is an excellent method, because the losses due to the wave-guide are on the order to 0.1 dB/m for RG(51)/U. At near-millimeter wavelengths (≥ 2 mm), however, waveguide losses are much larger. In the WR-4 waveguide, for example, the losses are on the order of 10 dB/m for frequency of 250 GHz. Clearly fundamental mode propagation in the near-millimeter band is unattractive for low-loss applications. Nevertheless, Lebedev (1990) used fundamental mode techniques up to 150 GHz, with estimated losses of 3 dB/m, which requires the use of compact structures. We note that "near-millimeter" is shorthand for the long-wavelength end of the far infrared regime, which we will define to be the wavelength region from 1000–100 μm (or 1–0.1 mm).

One way out of this difficulty is to abandon conventional microwave techniques for the near-millimeter band and, instead, to employ techniques common to the far infrared regime. Just as microwave techniques may be modeled as a high-frequency extension of transmission line tech-

---

[1] Present address: Department of Chemistry, Hurtig Hall, Northeastern University, Boston, Massachusetts.

ADVANCES IN MAGNETIC AND OPTICAL
RESONANCE, VOL. 19

niques, the quasioptical techniques of the far infrared are a natural extension downward in frequency from optical techniques. At higher frequencies and for those systems that have broadband frequency sources, quasioptical methods of radiation processing are an attractive alternative to microwave techniques.

We shall develop the theory necessary to understand quasioptics, but before that, it will be useful to consider factors that influence the choice of spectrometer components such as the magnet, the source, and the detector. In Section II we will give a brief review of the performance and characteristics of homodyne detectors. In our discussion of sources, we will discuss vacuum oscillators, such as the reflex klystron and backward wave oscillator, and solid-state sources, such as the Gunn diode. We will also discuss useful criteria for selecting a magnet.

The original far infrared (FIR) ESR spectrometer developed at Cornell is shown in Fig. 1. In several respects it is like a conventional ESR spectrometer in that it has a source, a resonator, and a detector, and it relies on magnetic field modulation to code the ESR signal for subsequent lock-in detection. Figure 2 shows a set of spectra collected over three decades of the rotational diffusion rate. The system is the spin probe cholestane (CSL) in the organic glass *o*-terphenyl (OTP). The range of diffusion rates corresponds to the motional narrowing region with $R \approx 10^9\ \mathrm{s}^{-1}$ at the top of the figure and the rigid limit with $R \approx 10^6\ \mathrm{s}^{-1}$ at the bottom of the figure. Note the excellent signal-to-noise ratio. We will present a detailed analysis of these data elsewhere (Earle *et al.*, 1996a). We will discuss the spectrometer sensitivity in detail in Section VIII. A reflection mode spectrometer based on the broadband techniques discussed in Secs. IX-XI (see also Earle and Freed, 1995) has been built and tested at 170 GHz (Earle *et al.*, 1996b). We find that the sensitivity of our new broadband bridge is higher than the transmission spectrometer shown in Fig. 1, which is consistent with the advantages of a reflection bridge as discussed in this chapter. Our recently completed reflection mode spectrometer has been used to study exchange processes in polyaniline (Tipikin, 1996). We show some illustrative spectra in Fig. 3. The signal to noise ratio is approximately a factor of 3 higher (or 7.5 higher when corrected for the frequency difference) for the reflection mode bridge compared to the transmission mode spectrometer (Earle *et al.*, 1996b).

The principal difference between this spectrometer and most conventional spectrometers is the use of quasioptical methods for the resonator and its coupling to the source and the detector. Our development of quasioptical theory will enable us to understand the advantages and limitations of quasioptics vis-à-vis microwave techniques. Fortunately, many concepts that are useful for understanding microwave propagation are

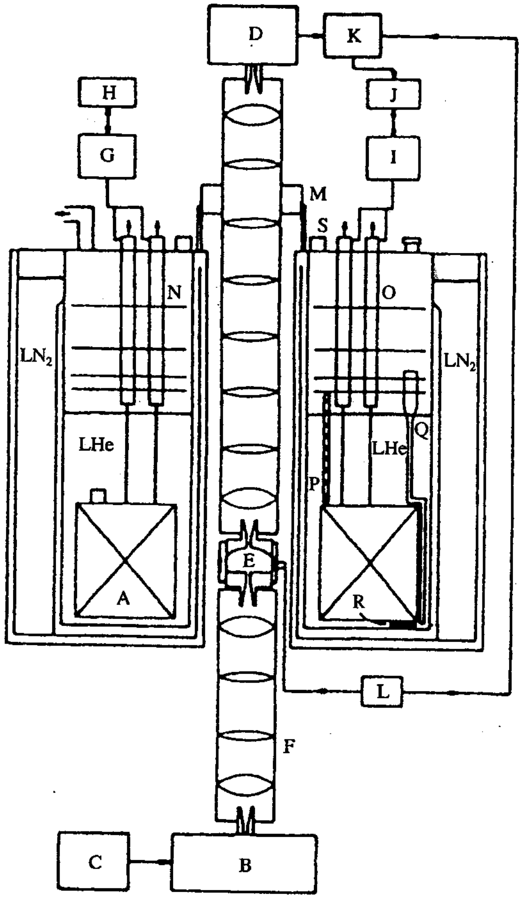

FIG. 1. 249.9-GHz FIR-ESR spectrometer. A, 9-T magnet and sweep coils; B, phase-locked 250-GHz source; C, 100-MHz master oscillator; D, Schottky diode detector; E, resonator and modulator coils; F, 250-GHz quasioptical waveguide; G, power supply for main coil (100 A); H, current ramp control for main magnet; I, power supply for sweep coil (50 A); J, OC spectrometer controller; K, lock-in amp for signal; L, field modulator and lock-in reference; M, Fabry–Pérot tuning screw; N, vapor-cooled leads for main solenoid; O, vapor-cooled leads for sweep coil; P, ^{4}He bath level indicator; Q, ^{4}He transfer tube; R, bath temperature thermometer; S, ^{4}He blow-off valves. [From Lynch *et al.* (1988), by permission of the AIP.]

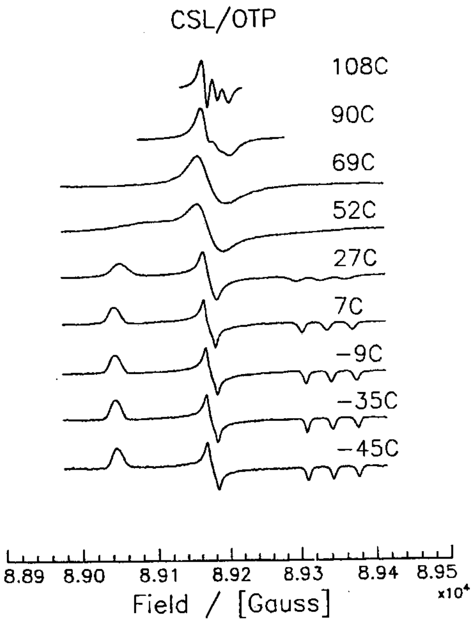

FIG. 2. Complete motional range of the cholestane spin probe (CSL) in the organic glass *o*-terphenyl (OTP). Note the excellent signal-to-noise ratio, The data were taken during an ESR study of several spin probes in *o*-terphenyl. The results of those experiments are discussed by Earle *et al.* (1996a).

useful in quasioptics as well, and we will exploit analogies where appropriate. In our discussion of adjustable finesse Fabry–Pérot resonators, for example, we will discuss the quasioptical equivalent of an induction mode resonator based on the X-band induction mode bridge of Teaney and Portis and coworkers (Teaney *et al.*, 1961; Portis and Teaney, 1958). An early version of a quasioptical spectrometer based on induction mode detection is briefly described in Smith (1995). See also Earle and Freed (1995).

Quasioptics is a formalism that is appropriate when geometrical optics is inadequate. Geometrical optics corresponds to a ray description of radiation that ignores its wave-like properties. This description is generally inappropriate if the radiation wavelength is not small. In the FIR, where wavelengths are of the order of 1 mm and optical structures have a scale size of a few centimeters, geometrical optics is invalid.

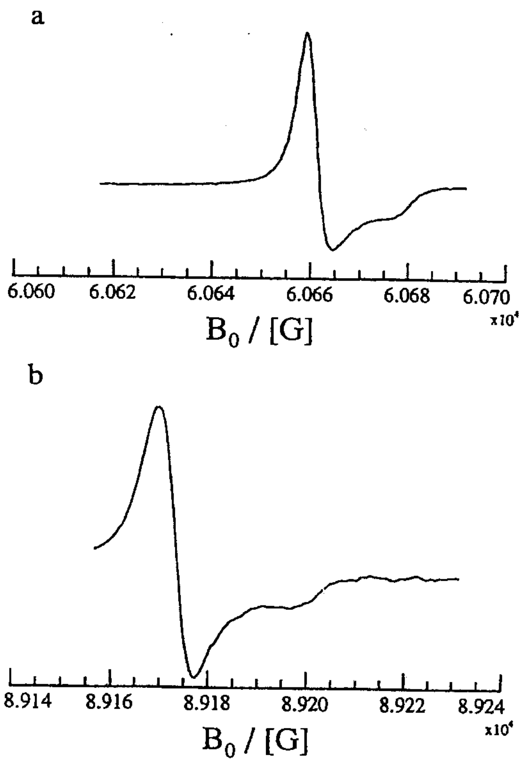

FIG. 3. Demonstration of the performance of the reflection mode spectrometer compared to the transmission mode spectrometer. (a) EPR spectrum of polyanilane at 170 GHz. The signal-to-noise ratio is 530:1. (b) EPR spectrum of polyaniline at 250 GHz. The signal to noise ratio is 180:1. [From Earle *et al.* (1996b), by permission of the AIP.]

We note that the term quasioptics implies that it is not sufficient to borrow familiar optical concepts, such as point focus, the lensmaker's equation, etc. without modification. In fact, diffraction plays a crucial role in characterizing system behavior. Fortunately, the quasioptics formalism allows us to avoid the time-consuming computation of diffraction integrals that would otherwise be necessary for a complete system analysis. We will concentrate instead on those aspects of quasioptics that are readily amenable to calculation in the paraxial approximation (see subsequent text). In particular, we will study the propagation of Gaussian beams.

A Gaussian beam is a modified plane wave whose amplitude decreases, not necessarily monotonically, as one moves radially away from the optical axis. The simplest, or fundamental, Gaussian beam has an $\exp(-\rho^2/w^2)$ radial dependence, where ρ is the radial distance from the optical axis and w is the $1/e$ radius of the electromagnetic field. The phase of a Gaussian beam also differs from that of a plane wave due to diffraction effects, as we will show subsequently.

The paraxial approximation is essentially a Taylor series expansion of an exact solution of the wave equation in powers of ρ/w, terminated at $(\rho/w)^2$, that allows us to exploit the rapid decay of a Gaussian beam away from the optical axis. We will develop a more precise criterion in the sequel. We will also show that the phase and amplitude modulation of the underlying plane wave structure of the electromagnetic field is a slowly varying function of distance from the point where the beam is launched.

Physically, the paraxial approximation limits attention to beams that are not rapidly diverging. We will establish criteria for the validity of the paraxial approximation while discussing typical applications and constraints. In this way, the reader will come to appreciate the advantages and limitations of quasioptics vis-à-vis microwave technology.

The principal features of quasioptics have been well reviewed (Martin and Bowen, 1993; Anan'ev, 1992). The collection of articles edited by LeSurf (1993), as well as his book (LeSurf, 1990), treats in great depth many of the topics that can only be touched on here, and we recommend both publications to all who are interested in a deeper understanding of the subject.

We will lay particular emphasis in this chapter on factors that influence the design and evaluation of high performance EPR spectrometers. This means that we must take into account the vector properties of the electromagnetic field, the effect of diffraction fringes, and the assumption of paraxial beams. We will then discuss approximations to the complete treatment that are specially useful in spectrometer design.

For the moment, we will content ourselves with the following qualitative remarks. Gaussian beams may be generated in a number of modes depending on the precise nature of the generator. Under the right circumstances, which we will quantify, it is possible to generate a beam whose **E** and **H** fields have a Gaussian profile as one moves radially away from the optical axis. We will call such a beam a fundamental Gaussian beam; it can be derived from the potential of radiating dipole as we will show. The modes of microwave waveguides, for example, may also be derived in such a manner. If the radiation pattern has side lobes (to use microwave parlance) or diffraction fringes (to use optical parlance), one may include higher order modes, that correspond to a multipole expansion of the field source.

The possibility of exciting higher order modes is well known to spectroscopists who use microwave techniques. There are also well-known techniques for minimizing the likelihood of such excitations. The same is true in the quasioptical case. We will show the conditions under which a given Gaussian beam may be propagated through an optical system without exciting higher order modes. We will endeavor to make clear at each step where departures from ideal cases may occur and what measures may be taken to ameliorate their effects.

[*Added in proof:* Since this chapter was originally completed in May 1995, many of the quasioptical ideas developed herein have now been realized in the development of a wideband (100–300 GHz) quasioptical reflection bridge by Earle *et al.* (1996b), and noted above. The original version of this chapter has been modified in order to update it in view of that work.]

II. Components

In this section we will discuss the considerations that influence the choice of source, detector, and magnet. Developments in source and detector technology, driven by applications in radar, communications, and radioastronomy, have been extremely important in the implementation of ESR spectroscopy at *W*-band (94 GHz) and higher frequency. The ready commercial availability of magnets of suitable homogeneity for high-resolution ESR work ($\approx 3 \times 10^{-6}$) for fields up to 9.5 T also has been instrumental for exploiting the advances in source and detector technology at frequencies above *Q*-band.

The choice of magnetic field is important because it constrains the frequency of operation. Higher fields mean higher resolution, in general, as in the NMR case, at least until the sources of inhomogeneous broadening such as *g*-strain broaden the line too severely. For systems that have *g* values close to the free electron value, however, this is not a severe limitation. Current magnet technology sets a limit of 9.5 T on the highest field that can be achieved at 4 K relatively inexpensively. It is possible to raise the maximum working field of such a magnet of 11.2 T by reducing the magnet temperature to 1.2 K; however, this generally requires sophisticated cryogen handling techniques. In such a system, a quench would be a spectacular event.

If still higher fields are desired, it is possible to use well-known, though expensive, super-conducting techniques up to 18 T, while maintaining high homogeneity. Such fields represent the state of the art for high-resolution nuclear magnetic resonance (NMR). The homogeneity that is required for such an NMR magnet is 0.1 Hz in 750 MHz, which corresponds to a homogeneity of approximately 1×10^{-9}. The constraints for ESR are not as severe: homogeneities of 3×10^{-6} are adequate for high-resolution work, and the cost can be reduced by specifying a lower homogeneity than is required for NMR. The problem is that shim fields are required to achieve even 3×10^{-6} homogeneity at 18 T, and the optimum value of the shimming field depends on the value of the field in the main coil. Given that field swept operation is still the most common mode of operation for high-field spectrometers to date, the optimum magnet configuration involves a trade-off between sweepability versus homogeneity above 9.5 T.

Based on all these considerations, we may take 9.5 T with a homogeneity of 3×10^{-6} as an upper limit of simple and economical operation. A magnetic field of 9.5 T corresponds to a frequency of approximately 270 GHz for a $g = 2$ system. The techniques that we will develop in this chapter may be extended up to 1 THz; we will limit our discussions and explicit examples to frequencies less than 300 GHz, where the analogies to conventional microwave techniques and components work best.

We will now consider the available options for generating and detecting radiation in the range of 100–300 GHz. The review of Blaney (1980) discusses in detail the general principles of detection methods in the wavelength region 3–0.3 mm, or 100–1000 GHz. His presentation is concerned mostly with the needs of radio astronomers, but he covers many topics of general interest. LeSurf (1990) covers similar material, but includes more recent developments than the Blaney review. LeSurf also discusses the options for sources in greater detail than Blaney. We cannot review sources and detectors extensively here. We will therefore limit our remarks to the most important points and refer the reader to the references for more in-depth discussion.

The sources of interest for CW radiation in the range 100–300 GHz are either solid-state devices based on negative dynamic resistance, such as the Gunn diode or IMPATT diode, or vacuum oscillators based on electron beam bunching, such as the reflex klystron or backward wave oscillator (BWO). The principal advantages of solid-state sources is that they are less expensive, do not require bulky high-voltage supplies or focusing magnets, and are very reliable. In terms of reliability, Gunn diodes are less susceptible to breakdown than IMPATT diodes; IMPATT diodes do provide more power than Gunn diodes, however. The drawback of solid-state devices, in general, is that the output power drops from approximately 50 mW at 100 GHz to approximately 1 mW at 300 GHz. Vacuum oscillators deliver higher powers than solid-state sources. A reflex klystron at 100 GHz will give about 1 W at a beam voltage of approximately 2–3 kV. A BWO at 100 GHz will give 10 W or more at a beam voltage of 4–8 kV. At higher frequencies, the power falls off dramatically, and BWOs only produce about 1 mW at 1 THz. The extended interaction oscillator (EIO) is a device that has a CW power of approximately 1 W near 200 GHz and a phase noise 120 dB below the carrier, or −120 dBc, at 100-kHz offset (Wong, 1989). The gyrotron is an extremely powerful device with kilowatt output powers. The noise performance of a gyrotron is not as good as an EIO. Nevertheless, gyrotrons may be used for dynamic nuclear polarization experiments in the near millimeter region (Griffin, 1995), and they will continue to be useful for those experiments that can exploit their intrinsically high powers. For ESR, a lower power BWO or EIO is probably preferable to a gyrotron.

At lower frequencies, vacuum oscillators have a broad electronic tuning range. The otherwise admirable performance of the EIO as a source must be balanced by the observation that its tuning range is limited to values as low as 1% at 220 GHz. Generally speaking, vacuum oscillators are difficult to obtain at frequencies above 220 GHz because commercial demand has been limited, hitherto. There is also much work to be done to optimize the performance of vacuum oscillators. One point in favor of high-frequency vacuum oscillators is that the operational lifetime of a BWO is 10–100 times that of a klystron (LeSurf, 1990), which may be an important consideration in building a spectrometer.

It is possible to build pulsed versions of the vacuum oscillators that can have variable pulsewidths and separations. The difficulty is in maintaining phase coherence between pulses. Solid-state sources may be switched to provide pulses, but the lower output powers limit the spectroscopist to selective pulses in many cases. As techniques become more advanced, pulse generation will become more and more common in near-millimeter band spectrometers. For the purposes of this chapter, however, we will limit our attention to CW sources.

The Cornell spectrometer is based on a phase-locked, CW, Gunn diode that has an output power of 3 mW at 250 GHz. The phase-lock circuitry is shown schematically in Lynch *et al.* (1988) and we will not comment on it further, except to note that the phase noise is −90 dBc at an offset of 100 kHz. The source is rugged, reliable, and very easy to use in practice.

There are several detection methods in the near-millimeter band in common use. We will limit attention to rectification and bolometric detection, because they are the most common methods for near-millimeter spectrometers built to date. Both methods rely on the intrinsic device properties to convert the signal information to a frequency range that can be conveniently processed.

LeSurf (1990) discussed bolometric detection in detail. It is important to note that the most common method of bolometric detection in the near-millimeter band is based on the use of the "hot-electron" bolometer, which is usually a chip of InSb, biased with a small current. At 4 K, the response time of the hot-electron bolometer is sufficiently fast that modulation frequencies of up to 1 MHz may be used. This value should be compared with a conventional bolometer, such as Ge or Si, which can only be modulated at a few hertz without sacrificing sensitivity. The relatively fast response time of a hot-electron bolometer means that it may also be used as a mixer, albeit with an intermediate frequency (IF) of only 1 MHz. When operated as a detector, an InSb bolometer has a noise equivalent power (LeSurf, 1990) NEP $\ll 10^{-12}$ W/$\sqrt{\text{Hz}}$.

When operated as a mixer, nonlinear devices detect signals at a frequency ν_S and mix them with a local oscillator at a frequency ν_{LO}. In general, the nonlinear element will generate sum and difference frequencies. One method of detection is to choose $\nu_S \approx \nu_{\text{LO}}$. In this way, the difference frequency $\nu_{\text{IF}} = |\nu_S - \nu_{\text{LO}}|$ can be chosen to be a convenient frequency, 1 GHz, say, and standard techniques may be used to amplify the down-converted signal at ν_{IF}. The amplifier that is used at ν_{IF} will have a bandwidth B_{IF}, which is typically 10% of ν_{IF}. In general, the down-conversion process is sensitive to frequency components in the lower side band from $\nu_{\text{LO}} - \nu_{\text{IF}} - (B_{\text{IF}}/2)$ to $\nu_{\text{LO}} - \nu_{\text{IF}} + (B_{\text{IF}}/2)$ and in the upper side band from $\nu_{\text{LO}} + \nu_{\text{IF}} - (B_{\text{IF}}/2)$ to $\nu_{\text{LO}} + \nu_{\text{IF}} + (B_{\text{IF}}/2)$. In the broadband radiometric experiments common to radioastronomy, one is often interested in the signal content in both side bands. For ESR spectroscopy and astronomical spectroscopy, it is usually the case that only one side band has signal information. The other side band will just down-convert local oscillator noise to ν_{IF}. The useful figure of merit for spectroscopy is the single side-band noise temperature, which can be approximated by doubling the quoted noise temperature of double side-band receivers designed for broadband radiometry. Given that spectroscopic signals only appear in one side band but noise appears in both channels, this is a fair comparison.

The double side-band receiver noise temperature has been measured for a variety of receivers based on several mixing strategies. An InSb hot-electron bolometer operated as a mixer was found to have a double side-band receiver noise temperature $T_R = 300$ K at 220 GHz (Blaney, 1980). This corresponds to an NEP $= 10^{-12}$ W/$\sqrt{\text{Hz}}$ referred to a predetection bandwidth of 100 GHz. The single frequency performance of mixer-based receivers does not generally match this performance, however (Boucher *et al.*, 1993).

Whisker contact diodes have much faster response times than InSb hot-electron bolometers and may be used as detectors or mixers. A good discussion of the behavior of near-millimeter band "cat-whisker" diodes may be found in Schneider (1982). When used as a mixer, the IF may be as high as several gigahertz, although conventional IFs are on the order of 1.8 GHz. The noise performance is not quite as good as an InSb mixer. LeSurf (1990) quotes a receiver noise temperature $T_R = 1000$ K for a Schottky diode mixer. When used as a detector, the noise is typically quoted under conditions that are more appropriate for radioastronomy than ESR spectroscopy. The Cornell 250-GHz spectrometer uses a GaAs whisker contact diode with a measured NEP $= 10^{-13}$ W/$\sqrt{\text{Hz}}$ are a modulation frequency of 100 kHz and a postdetection bandwidth of 1 Hz. This corresponds to our operation in transmission wherein the carrier feed-through acts as a homodyne bias, which significantly improves the observed NEP over what would be observed as a direct detector. We find the measured performance of an InSb hot electron bolometer has a signal-to-noise ratio that is approximately 4 times higher, under otherwise identical conditions, than a GaAs Schottky diode at 250 GHz. For routine use, we find it more convenient to use the GaAs Schottky diode, which is a room-temperature device, as opposed to the InSb bolometer, which requires a regular schedule of cryogen maintenance. We will show in Section VIII what implications this has for the minimum observable number of spins N_{min}.

The techniques that we discuss in this chapter apply to spectrometers that use mixers or detectors in the receiver. We will concentrate on detector-based systems because they are simpler in construction and concept. For a discussion of mixer-based receivers, we refer the reader to Blaney (1980), Goldsmith, (1982), and LeSurf (1990).

Improvements in the single side-band performance of a mixer-based receiver can be made by filtering the unwanted side band before it is down-converted in the mixer. Such a scheme, which is described in detail by Goldsmith (1982) is based on interferrometric techniques. We will not discuss single side-band filtering any further, except to note that it is a particularly apposite demonstration of the use of optical techniques to process the radiation in the spectrometer. We will discuss the use of interferometric techniques in Section IX as a means to realize a reflection mode spectrometer. These few examples indicate the flexibility of application of optical techniques to problems of instrument design in the FIR.

III. Mathematical Background

Quasioptics relies on free-space propagation of radiation, which is inherently low loss. Given that sources of FIR radiation are, generally speaking, less powerful than their microwave frequency counterparts, quasioptics is extremely attractive for propagating FIR radiation between the source, the resonator, and the detector. We will develop the mathematical background for describing Gaussian beams in this section with a view toward designing flexible and useful spectrometers.

In free space, an electromagnetic field of frequency ω is governed by the homogeneous vector Helmholtz wave equation

$$\nabla^2 \mathbf{F} + k^2 \mathbf{F} = 0 \tag{1}$$

where **F** is a vector function such as the electric field **E**, the magnetic field **H**, or the vector potential **A**. The quantity $k = \omega/c$ is the wavenumber of the free-space radiation.

It will prove useful in the sequel to use the hertz potentials (Born and Wolf, 1980, pp. 76–84) to describe the electromagnetic field. The hertz potentials also satisfy the homogeneous vector Helmholtz equation in free space. The advantage of the hertz potentials is that they display much higher symmetry than the conventional vector and scalar potentials. Furthermore, they may be written in a form that displays the paraxial approximation of quasioptics directly.

As we have stated, the **E** and **H** fields of a Gaussian beam have the same amplitude profile. The fields that are observed far away from a radiating dipole share this property without necessarily having a Gaussian profile. Near a radiating dipole, however, it is easy to distinguish whether the field has magnetic (electric) multipole or TE (TM) character. A linear superposition of the fields of a magnetic and electric multipole at right angles to one another will generate **E** and **H** fields with the desired symmetry. If the multipoles are in phase and have the same magnitude, the radiation modes are called hybrid or balanced *EH* modes. Monomode optical fibers, for example, typically use *EH* modes to propagate the radiation. An *EH* mode will have longitudinal **E** *and* **H** fields, because it is a superposition of TE and TM fields. We will show the conditions under which the longitudinal components may be considered negligible.

In order to make these qualitative statements more precise, we will derive all the electromagnetic field components of a fundamental Gaussian beam from two vector functions written in cylindrical coordinates as

$$\mathbf{\Pi}_e = (\hat{\rho}\cos\varphi - \hat{\varphi}\sin\varphi)u(\rho, z) \tag{2}$$

$$\mathbf{\Pi}_m = (\hat{\rho}\sin\varphi + \hat{\varphi}\cos\varphi)u(\rho, z) \tag{3}$$

where $\mathbf{\Pi}_e$ is the hertz potential of an electric dipole oriented along the polar axis $\varphi = 0$ and $\mathbf{\Pi}_m$ is the hertz potential of a magnetic dipole oriented along the axis defined by $\varphi = \pi/2$. Our choice of axes corresponds, in Cartesian coordinates, to an electric dipole with hertz potential $\mathbf{\Pi}_e$ oriented along the x axis and a magnetic dipole with hertz potential $\mathbf{\Pi}_m$ oriented along the y axis. The variables ρ, φ, and z are the standard cylindrical coordinates. The *scalar* function u is related to the Debye potentials (Debye, 1909; Bouwkamp and Casimir, 1954), which were first used in Debye's solution of the radiation pressure on a metallic sphere.

The choice

$$u = \exp\left(ik\sqrt{\rho^2 + z^2}\right)/\sqrt{\rho^2 + z^2} \tag{4}$$

in an exact solution of the vector Helmholtz equation (Deschamp, 1971; Born and Wolf, 1980, pp. 76–84) for the hertz potential of a dipole to within a constant. The time dependence $e^{-i\omega t}$ is assumed here and henceforth. In terms of the hertz potentials, the free-space electromagnetic fields are

$$\mathbf{B} = \mathbf{H} = \nabla \times (-ik\mathbf{\Pi}_e + \nabla \times \mathbf{\Pi}_m) \tag{5}$$

$$\mathbf{D} = \mathbf{E} = \nabla \times (+ik\mathbf{\Pi}_m + \nabla \times \mathbf{\Pi}_e) \tag{6}$$

Following the prescription of Deschamp (1971), we may substitute $z \rightarrow z - iz_0$, which represents a *complex* origin shift for the beam. The choice of a complex origin shift does not affect the validity of the solution; it is an analytic continuation of an exact solution of the Helmholtz equation for a complex source point. We will explore the significance of z_0 later. For the moment, we will merely assume that it is a large parameter. That assumption allows us to make a binomial expansion of u in powers of $(\rho/z - iz_0)^2$. The paraxial approximation consists of two parts. First, we only retain terms to order $(\rho/z - iz_0)^2$ in the exponent; second, we ignore the ρ dependence of the pre-exponential function. Both criteria are consistent with the assumption that z_0 is a large parameter.

In the paraxial approximation, therefore,

$$u \approx \frac{\exp(ik(z - iz_0))}{z - iz_0} \exp\left(ik \frac{\rho^2}{2(z - iz_0)^2}\right) \tag{7}$$

which may be rewritten, to within a constant, as

$$u = \frac{z_0 \exp(-(k\rho^2/2)z_0/(z^2 + z_0^2))}{\sqrt{z^2 + z_0^2}} \exp\left(i \frac{k\rho^2}{2} \frac{z}{z^2 + z_0^2}\right) \times \exp\left(-i \tan^{-1} \frac{z}{z_0}\right) \exp(ikz) \tag{8}$$

the pre-exponential factor shows that u decreases as z increases due to spreading of the beam. The exponential factor $\tan^{-1}(z/z_0)$ is the phase slip of the Gaussian beam with respect to a plane wave. When $z \approx z_0$ the phase slip is approximately $\pi/4$.

We may elucidate the meaning of z_0 by examining Eq. (8) at $z = 0$:

$$u(z=0) = \exp\left(-\frac{k\rho^2}{2z_0}\right) \equiv \exp\left(\frac{-\rho^2}{w_0^2}\right) \tag{9}$$

where w_0 is the $1/e$ radius of the dipole field at $z = 0$. In terms of w_0, we may make the identification

$$z_0 = \tfrac{1}{2}kw_0^2 \tag{10}$$

We have now found a physical meaning for the complex origin shift z_0: it characterizes the $1/e$ radius of the dipole radiation at $z = 0$. The Cornell FIR spectrometer uses $z_0 = 117$ mm, which corresponds to $w_0 = 6.7$ mm. Thus, even at $z = 0$, where $z - iz_0$ has its smallest magnitude, the quantity $(w_0/z_0)^2 = 3.28 \times 10^{-3}$ (which characterizes the paraxial approximation) is a small number. We may use the paraxial approximation with confidence to derive the properties of the fundamental Gaussian beam.

It is common to call w_0 the beam-waist radius. In the literature one often finds the phrase "at the beam waist," which refers to that value of z for which the function u has its minimum radial extent. For u defined by (8), this occurs at $z = 0$. The distance z_0 is called the confocal distance. When $z < z_0$ we say that the Gaussian beam is in the near field. When $z > z_0$, the Gaussian beam is in the far field. The majority of this chapter is concerned with the behavior of u in the range $0 < z < z_0$, the near-field region. The phase and amplitude of u is a complicated function of position in the near field. When $z \gg z_0$ and $\rho \ll z$ or when we are in the far field and the paraxial approximation is valid, it is straightforward to show that the asymptotic behavior of u approaches a diverging spherical wave from a point source at $z = 0$.

In the paraxial approximation, we may use Eqs. (5), (6), (8), and (10) to write expression for the transverse components of the electromagnetic field in terms of the hertz potentials as

$$\mathbf{B}_T = \mathbf{H}_T = (\hat{\rho}\sin\varphi + \hat{\varphi}\cos\varphi)2k^2u \tag{11}$$

$$\mathbf{D}_T = \mathbf{E}_T = (\hat{\rho}\cos\varphi - \hat{\varphi}\sin\varphi)2k^2u \tag{12}$$

to within an unimportant constant. One of the advantageous of the current approach, however, is that the vector Helmholtz theory gives us all components of the electromagnetic field. As we discussed above, the fields that we are studying should have longitudinal components, because they are superpositions of TE and TM modes. The longitudinal components of the electromagnetic field in the paraxial approximation using Eqs. (5), (6), (8), and (10) are

$$\mathbf{B}_L = \mathbf{H}_L = -\hat{z}\sin\varphi\,\frac{2k^2\rho}{z - iz_0}\,u \tag{13}$$

$$\mathbf{D}_L = \mathbf{E}_L = -\hat{z}\cos\varphi\,\frac{2k^2\rho}{z - iz_0}\,u \tag{14}$$

which is smaller than the transverse components by a scale factor ($kz_0 = 615$) for the Cornell spectrometer. The vector Helmholtz equations also generate a small cross-polarized component in the paraxial approximation, orthogonal to the transverse and longitudinal components, but small than the transverse components by a scale factor $(kz_0)^2 = 3.79 \times 10^5$.

The power radiated in the longitudinal portion of the electromagnetic field is approximately 60 dB lower than that in the transverse components assuming $kz_0 = 615$. The cross-polarized components are approximately 120 dB lower than the transverse components by the same assumption. It is a very good approximation, therefore, to neglect the longitudinal and cross-polarized components in our system. The importance of the vector approach, however, is that we may evaluate whether we may neglect the nontransverse portion of the electromagnetic field for a given w_0.

For a Gaussian beam, the fields of the radiating electric and magnetic multipoles satisfy the same boundary conditions (vanishing faster than $1/\rho$ as $\rho \to \infty$) so that the fields in the plane(s) defined by the transverse **E** (**H**) field and the optical axis are symmetric. It is difficult to generate a balanced hybrid mode in conventional smooth-walled metallic waveguide; instead, one may use a component called a *scalar horn*.

The scalar horn is discussed in the collection of papers edited by Love (1976). Basically, a scalar horn is a grooved circular waveguide with a small flare angle. The grooves act as radial shunt lines that insure the same boundary conditions for the **E** and **H** fields. An example of a device that uses radial shunt lines to modify waveguide properties is the $\lambda/4$ choke, which is a common feature of waveguide flanges at conventional microwave frequencies. For the narrow flare angles that are typically used, the phase variation over the aperture is modest, and one may assume that the beam-waist radius w_0 for a horn of given aperture diameter is 0.33 times the aperture diameter and is only weakly frequency dependent (Thomas, 1978).

We have used the much simpler conical horn on our detector and Fabry–Pérot resonator. We may estimate the ratio of the beam waists for a scalar and conical horn by calculating the ratio of their grains: $w_s/w_c = G_s/G_c$. For this purpose, we used the expressions for conical and scalar horn antennae given in Milligan (1985). For a conical horn, one should note that the beam patterns are quite different in the E and H planes. Using the parameters of the FIR-ESR horns, we find that the maximum phase error $\Delta = 0.08$. With Milligan's (1985) expressions and calculating the beam-waist ratio from the gains, we find that the beam radii of the two horns differ by less than 5%, which does not seem to be significant in practice.

We note that wall losses due to surface resistance in a smooth-walled horn can be significant above 300 GHz. Such losses reduce the field intensity near the walls of the horn and generate an aperture field that has more fundamental Gaussian character than might otherwise be expected (LeSurf, 1990, pp. 56–57).

A scalar horn or conical horn will generate side lobes (or diffraction fringes). In order to describe such features of a real beam, we need to consider higher order modes than the fundamental. Higher order modes are also important in discussing real resonators as we will show in Section VI.

In order to proceed, we will accept that the transverse components of the electromagnetic field are the only ones that are relevant in the problem on the basis of the exact calculation that we have performed for the fundamental Gaussian beam. Instead, we will use trial functions for u that will lead to self-consistent expressions for the transverse components of Gaussian beams of arbitrary order when substituted into the vector Helmholtz equation. The derivation is clearest for the fundamental. We will redrive the transverse field components of the fundamental Gaussian beam here. The deviation of higher order modes is outlined in the Appendix.

We write $u = \psi(\rho, z)e^{ikz}$, where we assume that $\psi(\rho, z)$ is a slowly varying amplitude and phase function as discussed in preceding text. We will model the (complex) phase modulation by a function $e^{iP(z)}$. The amplitude modulation will depend on z and ρ in order to account for beam growth. A suitable trial function is $e^{ik\rho^2/2q(z)}$, which is in the form of a diverging beam in the paraxial approximation, where $q(z)$ is a (complex) position-dependent radius of curvature. Putting the pieces together, we have $\psi(\rho, z) = \exp(i(P(z) + k\rho^2/2q(z)))$.

Writing the vector Helmholtz equation in cylindrical coordinates, using our trial function for u, and invoking the *Ansatz* that ψ is a slowly varying function of z in order to drop the term in $\partial^2\psi/\partial z^2$, we obtain an equation for P and q, namely,

$$2k\left(P' - \frac{i}{q}\right) + \frac{k^2\rho^2}{q^2}(1 - q') = 0 \tag{15}$$

where the prime indicates differentiation with respect to z. In order to satisfy Eq. (15) for all values of ρ and z, each term in parentheses must vanish separately, which leads to the following equations for P and q:

$$\begin{aligned} P' &= i/q \\ q' &= 1 \end{aligned} \tag{16}$$

Upon minding our Ps and qs, we obtain

$$q = z - iz_0 \tag{17}$$

$$-iP = \ln\left(1 + i\frac{z}{z_0}\right) \tag{18}$$

$$= \ln\sqrt{1 + \left(\frac{z}{z_0}\right)^2} + i\tan^{-1}\left(\frac{z}{z_0}\right) \tag{19}$$

where we have chosen the imaginary integration constant iz_0 guided by our experience with the exact solution in the paraxial approximation. In this way we see that q is a parameterization of the complex origin shift introduced previously that allowed us to make the paraxial approximation in the derivation of Eq. (8).

Setting $z_0 = \frac{1}{2}kw_0^2$ as before and using the definitions

$$w(z) = w_0\sqrt{1 + \left(\frac{z}{z_0}\right)^2} \tag{20}$$

$$R(z) = z\left(1 + \left(\frac{z}{z_0}\right)^2\right) \tag{21}$$

$$\Phi(z) = \tan^{-1}\left(\frac{z}{z_0}\right) \tag{22}$$

we may rewrite our trial function in terms of the Gaussian beam fundamental

$$u(\rho, z) = \frac{w_0}{w(z)}\exp\left(i(kz - \Phi(z)) - \frac{\rho^2}{w(z)^2} + \frac{ik\rho^2}{2R(z)}\right) \tag{23}$$

which is in the same form as Eq. (8) allowing for notational changes.

At this point, we have quantified the domain of validity of the paraxial approximation and established when we may neglect the nontransverse components of the Gaussian beam. We still need to examine our solution in more detail, because we have not yet addressed diffraction effects. This analysis is necessary because the wavelength of FIR radiation is of the same order of magnitude as the source extent (characterized by the beam waist).

We will test the consistency of our solution by evaluating the diffraction field of a Gaussian beam from a reference plane defined by $z = 0$. We will use the Huygens–Fresnel construction (Born and Wolf, 1980, pp. 370–386), where we treat each point on the wavefront in the reference plane as the source point for a secondary wavefront of the form $\exp(i\mathbf{k} \cdot \mathbf{r})/r$ and sum over all source points. If the diffracted field has the same functional form as the incident field, then we will have demonstrated that our solution is useful even in the presence of diffraction.

We may write an integral expression for the Huygens–Fresnel construction that embodies these considerations as follows (Anan'ev, 1992):

$$u(\rho, \varphi, z) = -\frac{ik}{2\pi} \int_0^\infty \rho_0 \, d\rho_0 \int_0^{2\pi} d\varphi_0 \, u(\rho_0, \varphi_0, 0) \frac{\exp(i\mathbf{k} \cdot (\boldsymbol{\rho} - \boldsymbol{\rho}_0))}{|\boldsymbol{\rho} - \boldsymbol{\rho}_0|} \tag{24}$$

where $\boldsymbol{\rho}$ is the vector that specifies the cylindrical coordinates of the field point and $\boldsymbol{\rho}_0$ is the vector that specifies the source point. The prefactor $-ik/2\pi$ is well known from diffraction theory (Born and Wolf, 1980, pp. 370–386) and ensures that the result has the correct units.

We may extend our discussion of diffraction effects to all Gaussian beam modes (not just the fundamental) by using the results of the Appendix, particularly Eq. (130) for $u(\rho_0, \varphi_0, 0)$. The kernel of the integrand in Eq. (24) may be rewritten in the paraxial approximation as

$$\frac{\exp(i\mathbf{k} \cdot (\boldsymbol{\rho} - \boldsymbol{\rho}_0))}{|\boldsymbol{\rho} - \boldsymbol{\rho}_0|} = \frac{\exp(ikz)}{z} \exp\left(\frac{ik\rho^2}{2z} + \frac{ik\rho_0^2}{2z} - \frac{ik\rho\rho_0 \cos(\varphi - \varphi_0)}{z} \right) \tag{25}$$

Collecting all of the ρ_0 independent factors outside the integrand, we may rewrite Eq. (24) as

$$u(\rho, \varphi, z) = (-1)^{(l+1)} \frac{z_0}{z} \exp(ikz) \exp(ik\rho^2/2z) \exp(il\varphi) \times \int_0^\infty dx \, x^{(l+1)} L_p^l(x^2) J_l(xy) \exp(-\beta x^2) \tag{26}$$

where we have used $z_0 = kw_0^2/2$, $x = \sqrt{2}\rho_0/w_0$, $y = w_0 k\rho/\sqrt{2}z$, and $\beta = (1 - iz_0/z)/2$. The φ_0 integration was performed by using an integral

representation of the Bessel function (Jackson, 1975):

$$J_m(x) = \frac{1}{2\pi i^m} \int_0^{2\pi} \exp(ix\cos\varphi - im\varphi) \, d\varphi \tag{27}$$

In the integral over x, or equivalently ρ_0, from 0 to ∞, we have assumed that the Gaussian function in the integrand has decayed sufficiently rapidly so that there is negligible error in taking the limit of integration to $x = \infty$, where the paraxial approximation would otherwise be inapplicable.

We have used scalar diffraction theory in this calculation, which is an approximation in two parts. The first part consists of approximating the electromagnetic field as a transverse field. We have derived the conditions under which it is permissible to do so. In the Appendix, we discuss the conditions under which it is possible to replace the vector Helmholtz equation by the scalar Helmholtz equation for transverse fields. In a sense, we have reduced the problem to a solution of the scalar Helmholtz equation. The second part of the approximation consists of exploiting the reduction of the vector Helmholtz equation to a scalar Helmholtz equation. Scalar diffraction theory is based on the scalar Helmholtz equation. Hence, when it is permissible to neglect the longitudinal and cross-polarized components of the Gaussian beam, we may use solutions of the scalar Helmholtz equation for transverse fields and may take over the results of scalar diffraction theory with confidence for this special case.

We may use Eq. (140) from the appendix with $\alpha = 1$, $\nu = l$, $n = p$, and x, y, and β defined previously to evaluate the integral in Eq. (26):

$$(-i)^{l+1} \int_0^\infty x^{l+1} \exp(-\beta x^2) L_p^l(x^2) J_l(xy) \, dx = \frac{[2i(\beta - 1)]^p}{[2i\beta]^{(p+l+1)}} y^l \exp\left(-\frac{y^2}{4\beta}\right) L_p^l\left[\frac{y^2}{4\beta(1-\beta)}\right] \tag{28}$$

where we have included the phase factos $(-i)^{l+1}$ from Eq. (26) for future convenience.

The first factor on the right-hand side of Eq. (28) may be rewritten as

$$\frac{[2i(\beta - 1)]^p}{[2i\beta]^{(p+l+1)}} = \frac{\exp(-i(2p + l + 1)\tan^{-1}(z/z_0))}{(2|\beta|)^{l+1}} \tag{29}$$

It is also possible to combine the Gaussian $\exp(-y^2/4\beta)$ with the prefactor $\exp(ik\rho^2/2z)$ from Eq. (26) to obtain

$$\exp\left(\frac{ik\rho^2}{2z} - \frac{y^2}{4\beta}\right) = \exp\left(\frac{ik\rho^2}{4\beta z}\right) \tag{30}$$

Finally, the function $ik\rho^2/4\beta z$ may be rewritten as $-\rho^2/w(z)^2 + ik\rho^2/2R(z)$, where $w(z)$ and $R(z)$ are define in Eqs. (20) and (21).

In this way, Eq. (28) may be rewritten as

$$(-i)^{l+1}\exp\left(\frac{ik\rho^2}{2z}\right)\int_0^\infty x^{l+1}\exp(-\beta x^2)L_p^l(x^2)J_l(xy)\,dx$$
$$= \frac{\exp(-i(2p+l+1)\tan^{-1}(z/z_0))}{(2|\beta|)}\left(\frac{y}{|\beta|}\right)^l \exp\left(\frac{-y^2}{4\beta}\right)L_p^l\left[\frac{y^2}{4|\beta|^2}\right] \tag{31}$$

Using our definitions of y and β, we may use Eq. (31) to simplify Eq. (26) to its final form

$$u(\rho,\varphi,z) = \frac{w_0}{w(z)}\left(\sqrt{2}\,\frac{\rho}{w(z)}\right)^l L_p^l\left(2\frac{\rho^2}{w^2(z)}\right)\exp\left(-\left(\frac{\rho}{w(z)}\right)^2\right)$$
$$\times \exp\left(i\left[kz + l\varphi - (2p+l+1)\tan^{-1}\left(\frac{z}{z_0}\right) + \frac{k\rho^2}{2R(z)}\right]\right) \tag{32}$$

which is in the form of Eq. (130), the expression for a general Gaussian beam mode. Note that the term $\exp(-i(2p + l + 1)\tan^{-1}(z/z_0))$ means that a beam that consists of the fundamental plus higher order modes will be dispersive. For the standing wave case this is clearly demonstrated in Fig. 4, where the various higher order modes appear as shoulders on the main resonance corresponding to the fundamental mode. We will discuss higher order modes more thoroughly in the sequel.

We have now shown that the functional form of all Gaussian beam modes is preserved even in the presence of diffraction, subject only to the validity of the paraxial approximation and the assumption of transverse fields. All of our results are consistent, therefore, with the assumption that a Gaussian beam is a modulated plane wave, where the modulation function is a slowly varying function of position. It is also possible to quantify the domain of validity of the paraxial approximation (Martin and Bowen, 1993). In the far field ($z \gg z_0$) it is possible to use the method of steepest descent to evaluate the integral in Eq. (24). The result is that we may neglect effects due to the breakdown of the paraxial assumption as long as $kw_0 > 6$. When higher order modes are important, the appropriate criterion is (Martin and Bowen, 1993) $kw_0 > 6(n/2)^{1/2}$, where n is the mode number. The Cornell group uses a system beam waist $w_0 = 6.7$ mm, which implies $kw_0 \approx 35$ for a wavelength of 1.2 mm.

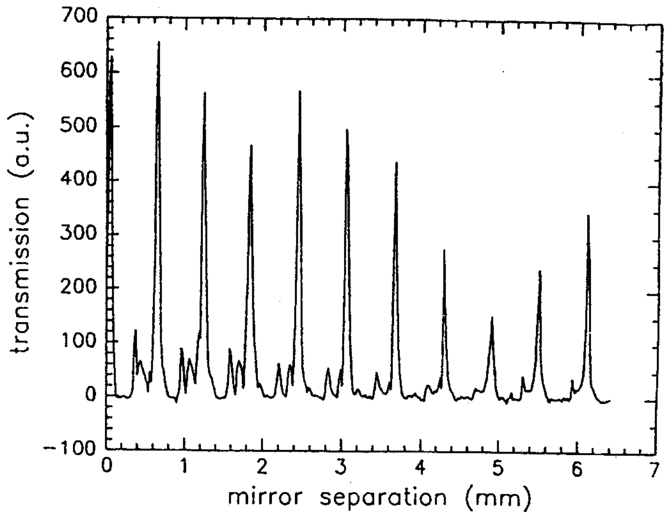

FIG. 4. Scan of cavity modes in the presence of a sample and sample holder. The most intense resonances are the longitudinal resonances, which are the resonances of the fundamental Gaussian beam. Radial and azimuthal modes are also present and appear as shoulders on the longitudinal resonances. Note that the higher order radial and azimuthal modes are slightly dispersive.

IV. Quasioptical Beam Guides

In this section, we discuss general features of beam guide systems that are important when the cross-sectional area of the beam must be kept to a finite diameter. This is an important consideration in spectrometer design. EPR spectrometers in the FIR will typically require superconducting magnets with finite warm bore sizes to study $g = 2$ systems, for example (cf. Fig. 1). We will discuss the conditions that are necessary for a beam to have free-space propagation characteristics in systems with finite cross-sectional areas. .

The Gaussian beam of Eq. (8) has a radial amplitude dependence $\exp(-\rho^2/w^2(z))$, where $w(z)$ is given by Eq. (20). The quantity $w(z)$ is called the beam radius; its minimum value—the beam waist w_0—occurs at $z = 0$. Conventionally, $z = 0$ is referred to the beam waist; the context makes it clear whether w_0 or $z = 0$ is being discussed. As z increases, $w(z)$ increases monotonically. It is easy to show from Eq. (20) that $\lim_{z\to\infty} w(z)/z = \lambda/\pi w_0$, the asymptote of a hyperbola. We call the quantity $\tan^{-1}(\lambda/\pi w_0)$ the asymptotic beam growth angle.

In order to limit the growth of the beam, we use lenses to refocus the Gaussian beam. Generally speaking, an ideal lens or conic section reflector introduces a phase delay that varies quadratically with distance from the optical axis. Upon passage through a lens or reflection from a conic section reflector, the quadratic phase delay changes the radius of curvature of the exiting beam.

The focal length of a quadratic, phase transforming, optical element is given by the formula

$$\frac{1}{R_i} - \frac{1}{R_e} = \frac{1}{f} \tag{33}$$

where R_i is the radius of curvature of the incident beam, R_e is the radius of curvature of the exiting beam, and f is the focal length of the optical element, which may be positive or negative. Conventionally, the radius of curvature is taken as positive if the beam is diverging and negative if it is converging.

We would like to make some general comments on lens design. First, the optimum surface for lenses if not spherical, but hyperboloidal (Moore, 1988). The general design procedure is given, for example, Kraus (1950). We note that the assumption of a point source in Kraus' design procedure is admirably suited to the far-field ($z \gg z_0$) behavior of a Gaussian beam. If the refractive surface is in the near field ($z \ll z_0$) of the beam waist, one may use the general procedure given in Risser (1949) to make the appropriate phase corrections. Second, there will be a dielectric mismatch at the refractive surface, which may be modeled as an impedance discontinuity in a transmission line. For Teflon, which has an index of refraction of $n = 1.44$ in the FIR (Degenford and Coleman, 1966), the reflection coefficient $\rho = (n-1)/(n+1)$, which implies that roughly 3% of incident power is reflected from each air–dielectric interface: $P_r \approx \rho^2 P_i$, where P_r is the reflected power and P_i is the incident power. For narrow-band systems, it is possible to design lenses that have extremely low reflection losses (Padman, 1979). As a concrete example, the insertion loss of the lenses that are used in the Cornell spectrometer, which includes losses in the lens material as well as reflection losses, is 0.1 dB.

Our primary use of reflectors has been as elements in a Fabry–Pérot resonator (cf. Section VI). If reflectors are used as focusing elements instead of lenses, it is common to use nonnormal incidence to avoid truncation losses. The choice of reflecting optics with nonnormal incidence does introduce aberrations in the reflected field, the most serious of which is *coma* (Murphy, 1987).

In an optical system with nonnegligible coma, a point object produces an image that has a comet-like tail, whence the name *coma*. It is possible to arrange pairs of reflectors, however, so that aberrations cancel or nearly cancel (Murphy, 1987). Our recent work (Earle *et al.*, 1996b) exploits the properties of paired mirrors to maintain the mode purity of the Gaussian beam. The reader is referred to that work for a more detailed discussion of the optical layout. Here we will not consider the effect of astigmatism, that is, different focal lengths in the *xz* or *yz* planes, although it is possible to account for such effects (Anan'ev, 1992; Murphy, 1987).

The expressions derived in the foregoing text for the behavior of a Gaussian beam tacitly assumed that truncation effects could be ignored; that is, the expressions were derived for an infinite aperture system. Any physical system, of course, consists of elements of finite extent. The question to consider, then, is under what conditions those elements may be approximated by ideal elements.

For any beam incident on an aperture of finite extent, we may define the edge taper T_E as the ratio of power on-axis to the power level at a given radius off-axis. One may approximate the power density for a fundamental Gaussian beam by u^*u, where u is given by Eq. (23). For such a beam, $T_E = 20\log(\exp(-(\rho/w)^2))$. Numerical evaluation of the diffraction integral for a circular aperture of radius $\rho = a$ illuminated by a Gaussian beam (Campbell and DeShazer, 1969) of radius w suggests that the maximum discrepancy between the scattered near-field angular distribution and the pure Gaussian beam is 4% when $a/w = 2$. The far-field behavior seems to be less sensitive (Schell and Tyras, 1971) to truncation effects, which appear mainly in low level side lobes (or diffraction fringes). The principal effect seems to be on the width of the Gaussian envelope (Goldsmith, 1982). Given $a/w = 2$, the ratio of the truncated to nontruncated beam radius is 1.03.

In order to understand why this ratio is greater than unity, we must consider that the truncated beam contains higher order modes than the fundamental because of diffraction from the finite aperture. As the aperture is stopped down (made smaller), the diffraction fringes become better resolved. For aperture diameters that are not too small, however, the principal effect on the beam is an apparent broadening of the beam radius due to unresolved diffraction fringes with significant intensity away from the optical axis.

Inserting $a/w = 2$ into the expression for the edge taper, yields $T_E = -35$ dB. Goldsmith (1982) has compiled a table that shows the effect of reducing the edge taper on the full width at half maximum (FWHM) asymptotic beam growth angle. For an edge taper of -25 dB, the beam radius is roughly 10% larger than the untruncated value, which seems to be the limit on the edge taper that one may use without having excessive diffractive beam growth.

Finally, even if the aperture is sufficiently large that diffractive beam growth is not a problem, small focal lengths can cause significant phase and amplitude distortions (Goldsmith, 1982) if the ratio of the focal length to the aperture diameter $f/D < 0.6$. The quantity f/D is conventionally known as the f-number or $f/\#$ of an optical element. For reflectors, cross-polarization can be significant for small $f/\#$ and large angles of incidence as described by Chu and Turrin (1973). The state of the art in the near-millimeter band seems to be polarization isolation at the 30-dB level (Moore, 1988), which is a reasonable specification to strive for in the reflection mode spectrometer to be discussed in Section IX.

The FIR-ESR spectrometer, in its transmission mode configuration, uses conical horns and many lenses without seriously compromising performance. In the future, however, as more elements are added, it will be important to reevaluate the use of nonoptimal components.

V. Design Criteria for Beam Guides

In this section, we will discuss design criteria for beam guides from a slightly generalized point of view. A common problem in quasioptics is calculating the focal length of a phase-transforming lens or reflector to transform an input beam with a given beam waist into an output beam with a different beam waist. Coupling into and out of resonators is an example of such a process. Matching to a detector input is also a common example. With care, it is possible to achieve coupling losses as low as 0.15 dB (Wylde, 1984) or better. For those situations where signal power is at a premium, attention to details such as good coupling will yield important benefits.

It is possible to include phase transformers in scalar diffraction theory. The calculations are lengthy, however, and we refer the reader to Anan'ev (1992) and Martin and Bowen (1993) for details. An alternative approach exists that is equivalent to the transfer matrix method of geometrical optics, although the results are justifiable in terms of diffraction theory (Anan'ev, 1992; Martin and Bowen, 1993). The formalism is discussed, for example, in Hecht and Zajac (1979, pp. 171–175) and we will briefly outline the necessary results.

In a ray descriptions of optics, one can predict the performance of an optical system by tracing the path of rays through the system. Given a ray whose vertex is displaced from the optical axis by y_{in} and whose slope is given by α_{in}, it is possible to find the output displacement y_{out} and slope α_{out} after passage through the system by computing

$$\begin{pmatrix} y_{\text{out}} \\ \alpha_{\text{out}} \end{pmatrix} = \begin{pmatrix} A & B \\ C & D \end{pmatrix} \begin{pmatrix} y_{\text{in}} \\ \alpha_{\text{in}} \end{pmatrix} \tag{34}$$

where the matrix $\begin{pmatrix} A & B \\ C & D \end{pmatrix}$ is called the system transfer matrix $\mathcal{T}$. The elements of $\mathcal{T}$ are known for various optical elements (Hecht and Zajac, 1979, pp. 171–175) such as lenses or free-space propagation, and $\mathcal{T}$ for a system of such elements may be found by matrix multiplication:

$$\begin{pmatrix} A & B \\ C & D \end{pmatrix} = \begin{pmatrix} A_n & B_n \\ C_n & D_n \end{pmatrix} \cdots \begin{pmatrix} A_2 & B_2 \\ C_2 & D_2 \end{pmatrix} \begin{pmatrix} A_1 & B_1 \\ C_1 & D_1 \end{pmatrix} \tag{35}$$

where the ray encounters elements $1, 2, \ldots, n$ in order and the transfer matrix for optical element i is given by $\begin{pmatrix} A_i & B_i \\ C_i & D_i \end{pmatrix}$. We will give a specific example of the formalism applied to a Gaussian beam transformed by a lens.

Within the paraxial approximation for Gaussian beams, Kogelnik (1965) has shown that the analog of the transfer matrix formalism is the $ABCD$ law for the parameter $q = z - iz_0$ [cf. Eq. (17)]; that is, $q_{\text{out}} = (Aq_{\text{in}} + B)/(Cq_{\text{in}} + D)$, where the $ABCD$ coefficients may be taken from the corresponding optical system transfer matrix in the form

$$\mathcal{T} = \begin{pmatrix} A & B \\ C & D \end{pmatrix} \tag{36}$$

A common problem in quasioptics is transforming the beam waist at the output of the source to a more convenient value for propagation over extended distances. The beam waist at the output of a scalar horn of aperture radius a is (Wylde, 1984) $w_0 = 0.6435a$. Scalar horns are usually made short for ease of fabrication so that w_0 is small, however. The asymptotic beam growth angle $\tan^{-1}(\lambda/\pi w_0)$ for a scalar horn is approximately 10° as a rule of thumb in the near-millimeter region. If one transforms the beam waist to a larger value, the asymptotic growth angle decreases and one may space focusing lenses farther apart (as we will show subsequently), which reduces the insertion loss of quasioptics. Transforming the beam waist from 2.0 to 6.7 mm, for example, will reduce the asymptotic beam growth angle to 3.3°, which allows the lenses of our quasioptical system to be spaced every 235 mm at 250 GHz (see subsequent text). If the beam waist is 2.0 mm, the lenses must be spaced every 21 mm, which leads to insertion losses an order of magnitude higher, in addition to the problems caused by small $f/\#$s.

Let us now calculate the distances and focal length required to transform the beam waist from one value to another. At each beam waist, q is pure imaginary: $q_1 = -i\pi w_1^2\lambda$ and $q_2 = -i\pi w_2^2/\lambda$.

The *ABCD* matrix may be found from a knowledge of the transfer matrices (Hecht and Zajac, 1979, pp. 171–175) for translation through a distance d and passage through a lens of focal length f, namely,

$$T(d) = \begin{pmatrix} 1 & d \\ 0 & 1 \end{pmatrix} \tag{37}$$

$$R(f) = \begin{pmatrix} 1 & 0 \\ -1/f & 1 \end{pmatrix} \tag{38}$$

For this case, the system transfer matrix $\mathscr{T} = T(d_2)R(f)T(d_1)$. Applying the *ABCD* law yields

$$q_2 = \frac{(1 - d_2/f)q_1 + (d_1 + d_2 - d_1 d_2/f)}{-q_1/f + (1 - d_1/f)} \tag{39}$$

where d_1 and d_2 are the distances to the input and output beam waists; hence d_1 and d_2 are the quasioptical equivalents of the geometrical optics image and object distances. Equating the real and imaginary parts of Eq. (39) leads to two equations for d_1 and d_2. Solving for d_1 and d_2 separately, and introducing the parameter $f_0 = \pi w_1 w_2/\lambda$ allows us to write

$$d_1 = f \pm \frac{w_1}{w_2}\sqrt{f^2 - f_0^2} \tag{40}$$

$$d_2 = f \pm \frac{w_2}{w_1}\sqrt{f^2 - f_0^2} \tag{41}$$

Note that the parameter f_0 is equal to the geometric mean of the two beam parameters z_1 and z_2. If we take the point of view that a Gaussian beam of beam waist w_0 is a transmission line of charactieristic impedance z, then a device that matches a transmission line of impedance z_1 to a line of impedance z_2 will require a quarter wavelength section of impedance $\sqrt{z_1 z_2}$. Note that if the focal length of the mode-matching lens is f_0, then $d_1 = d_2$ and we may think of the length of the matching segment as $2f_0 = 2\sqrt{z_1 z_2}$. The analogy is more complicated if the focal length is different from f_0. In fact, a lens of any focal length greater than f_0 will do, subject to the caveats outlined previously. The conceptual simplicity of the transmission line model is very useful, however.

If we imagine a series of N lenses of focal length $f_0 = z_0$ separated by $2f_0$ such that the beam waist occurs midway between any pair of lenses, then we may model the optical system as a transmission line of length $2Nz$ and characteristic impedance z. It is conventional to work with a dimensionless impedance in transmission line work; therefore one may define a normalized impedance $\zeta = z/\lambda$, although any convention would suffice, as long as it was used consistently.

A very useful and succinct discussion of optimizing lenses for transmission over relatively long distances is given by Goldsmith (1992). The basic result is that the maximum possible distance between two focusing elements for a Gaussian beam is twice the confocal distance, $d = 2z_0$, where $z_0 = kw_0^2/2$ and w_0 is the beam waist. In Section IV, we discussed the minimum aperture possible for propagating undistorted Gaussian beams and found the condition $a/w > 2$, where a is the lens aperture radius and w is the beam radius at the lens aperture. If we set $z = z_0$ in Eq. (20), we find $w(z_0) = \sqrt{2}w_0$ at the lens aperture. The distance d is therefore determined by quasioptical constraints to be $d \le ka^2/8$. In terms of the aperature diameter $D = 2a$ and the wavelength $k = 2\pi/\lambda$, we find

$$d \le \frac{\pi D^2}{16\lambda} \tag{42}$$

The Cornell FIR-ESR transmission spectometer uses $D = 37.9$ mm, $w_0 = 6.7$ mm, $\lambda = 1.2$ mm, and $z_0 = kw_0^2/2 = 117.5$ mm, which results in $d = 235$ mm. The necessary focal lengths for the optics may be found from Eqs. (40) and (41); we find $f = z_0$. The geometrical optics result for a point source at position z_0 away from the lens imaged to a point z_0 on the other side of the lens is $f = 2z_0$ as one may verify from Eq. (33).

In this case, properly accounting for diffraction effects reduces the required focal length by a factor of 2. The distance z_0 is called the confocal distance, which we introduced in Section III. It separated the near-field $(z \ll z_0)$ and far-field $(z \gg z_0)$ regions, or equivalently, the Fresnel and Fraunhofer diffraction regions.

VI. Fabry–Pérot Resonators

We have chosen to develop the quasioptical theory needed for understanding the spectrometer by considering first the properties of lenses and reflectors. In the analysis of resonators, a very fruitful approach is to "unfold" the multiple reflections of the resonator into a series of lenses in circular apertures spaced by the mirror separation for a confocal resonator (Kogelnik and Li, 1966). The semiconfocal resonator is a special case of the confocal resonator. We use a flat mirror, which images the curved mirror at minus the mirror separation. In such a resonator, it is impossible

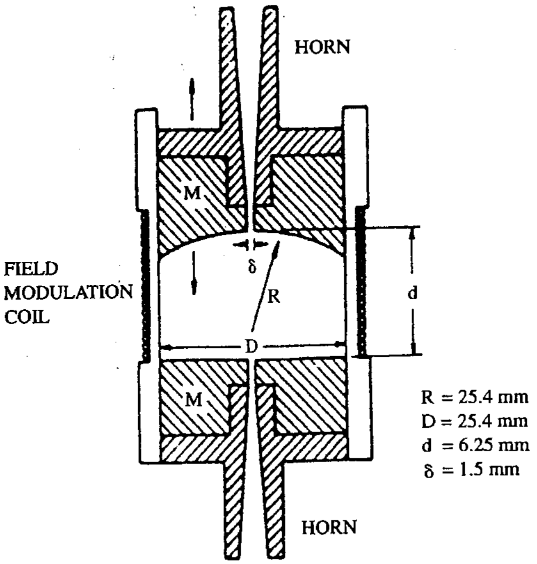

FIG. 5. FIR-ESR semiconfocal resonator showing horn coupling. The beam-waist radius in the resonator is 2.2 mm. [From Lynch *et al.* (1988), by permission of the AIP.]

to have an antinode of the E field at the beam waist. The FIR-ESR resonator is shown in Fig. 5.

In microwave work, one specifies the performance of a cavity by its quality factor, which is typically defined as $Q = \omega_0/\Delta\omega$, where ω_0 is the central frequency of the resonance and $\Delta\omega$ is the power FWHM. In order to develop an expression for the Q of a semiconfocal Fabry–Pérot resonator, we must examine the behavior of the Gaussian beam given by Eq. (130) between two mirrors. One may readily derive an eigenvalue equation for the resonator by considering that the field in the resonator consists of the superposition of a traveling wave in the $+z$ and $-z$ directions and forcing the resultant standing wave E field to vanish on both mirrors. Note that a traveling wave solution in the $+z$ direction, $(\mathbf{E}, \mathbf{H})$, has a complementary solution in the $-z$ direction, $(\mathbf{E}^*, -\mathbf{H}^*)$. If one sets $E_x = u$, then a standing wave that vanishes at $z = 0$ may be constructed from $E_{\text{cav}} = E_x = (u - u^*)/2i$. Following the convention given above, $H_{\text{cav}} = H_y = (u + u^*)/2$. The extra factor of $-i$ in the defining relation for E indicates that H leads E by a quarter period: the field energy shuttles back and forth between the electric and magnetic energy densities, as it should for an energy-storing element. In order to determine the beam waist in the resonator, we choose the local radius of curvature, $R(d) = R_0$, where R_0 is the radius of curvature of the spherical mirror and d is the mirror separation. Using Eq. (21) and solving for the beam waist, we find

$$w_0^2 = \frac{\lambda}{\pi}\sqrt{d(R_0 - d)} \tag{43}$$

In the Cornell spectrometer, $R_0 = 2d = 25.4$ mm is possible mode of operation, although it is not ideal as we will show subsequently. For that case, $w_0 = 2.2$ mm. We choose such a small beam waist in order to concentrate the available power near the optical axis and enhance the B_1 field for samples on the optical axis. We will show in the following text that $B_1 \propto 1/w_0$.

For fixed frequency, only a discrete set of d values causes the resonator to resonate. Recall that the resonance condition obtains when the phase shift between the mirrors is an integral multiple of π, say $q\pi$, where q is an integer. The phase of an arbitrary Gaussian beam mode is given by the argument of u from Eq. (130) in the Appendix. We may write the resonance condition as

$$kd - (2p + l + 1)\tan^{-1}(d/z_0) = q\pi \tag{44}$$

where q is the longitudinal mode number equal to the number of antinodes of the standing wave pattern, l is the azimuthal mode number, and p is the radial mode number (cf. the Appendix). The fundamental Gaussian mode corresponds to $l = p = 0$. Note that the separation between longitudinal resonances measured as a frequency is $\nu_0 = c/2d$. Using $\omega/k = c$ and $\omega = 2\pi\nu$ we may solve for the resonance frequency of the resonator, namely,

$$\frac{\nu}{\nu_0} = q + \frac{1}{2\pi}(2p + l + 1)\cos^{-1}\left(1 - \frac{2d}{R_0}\right) \tag{45}$$

where we have used the identity (Chantry, 1984, Vol. 1, p. 70) $2\tan^{-1}\sqrt{a/(2b - a)} = \cos^{-1}(1 - a/b)$. The second term on the right-hand side of Eq. (45) causes the mode pattern of the resonator to be dispersive, that is, modes p or $l \neq 0$ are resonant at a different mirror separation than the fundamental. This is clearly demonstrated in Fig. 4. In addition, the modes are degenerate at the confocal separation, $d = R_0/2$. When $d = R_0/2$, Eq. (45) becomes $\nu/\nu_0 = q + (2l + p + 1)/4$. If $2l + p$ increases (decreases) by 4, it is degenerate with the longitudinal mode $q - 1$ $(q + 1)$. Even though the smallest beam waist occurs for the confocal separation, it is not common to operate a resonator at that mirror separation, because the mode degeneracy leads to easy mode conversion and higher losses.

Having found an expression for the eigenfrequencies of the resonator, it now remains to find expressions for the diffraction losses and electrical losses in order to calculate the Q. Slepian (1964) developed asymptotic expansions for the phase shifts and diffraction losses of various mirror shapes, which may be parameterized by Fresnel zone number, $N = a_1 a_2 / d\lambda$, where a_i $(i = 1, 2)$ is a mirror radius, d is the mirror separation, and λ is the wavelength. If we take a_1 as an aperture radius and λ as the wavelength, the boundaries of the Fresnel diffraction zones occur at the angles $\tan^{-1}(N\lambda/a_1)$, where $N = 1, 2 \ldots$. If we set a screen at a distance d from the aperture, the Nth Fresnel diffraction zone occurs at the angle $\tan^{-1}(a_2/d)$. Comparing arguments of the $\tan^{-1}$ functions, we arrive at the condition

$$N = \frac{a_1 a_2}{\lambda d} \tag{46}$$

The argument is unaffected by interchanging a_1 and a_2. We may use Babinet's principle (Born and Wolf, 1980, pp. 370–386) to replace the apertures with mirrors of radii a_1 and a_2. The case $N = 1$ corresponds to both mirrors being illuminated by the first Fresnel diffraction zone. Reducing N by decreasing the radii a_1 and a_2 is a convenient way to filter the higher order radial p and azimuthal l modes. Basically, the higher order modes are truncated by the finite mirror radii. Knowing the Fresnel zone number for a particular set of mirrors and the mode numbers, we may calculate the diffraction loss parameter (Slepian, 1964)

$$\alpha = \frac{2\pi(8\pi N)^{2p+l+1} e^{-4\pi N}}{p!(p+l+1)!}\left[1 + O\left(\frac{1}{2\pi N}\right)\right] \tag{47}$$

The total energy stored in the resonator is proportional to the geometrical phase shift of the cavity, kd, where d is the mirror separation, whence we may derive a diffraction Q, $Q_D = 2\pi d/\lambda\alpha$. In general, one must also consider electrical losses (which contribute to the unloaded Q), sample absorption and scattering (which contribute to the sample Q, Q_χ), and resonator coupling (which contributes to the radiation Q, Q_R). Q_L, the loaded Q, of the cavity, may therefore be written as a sum of terms

$$\frac{1}{Q_L} = \frac{\lambda\alpha}{2\pi d} + \frac{1}{Q_U} + \frac{1}{Q_\chi} + \frac{1}{Q_R} \tag{48}$$

Q_χ, the sample Q, contains an EPR resonant contribution Q_{EPR} and a nonresonant contribution Q_{optical}, which is determined by the optical properties of the sample: its thickness and index of refraction n. A slab of dielectric may be thought of as a Fabry–Pérot resonator (hence Q_{optical}). We discuss in Section X how to treat a compound Fabry–Pérot resonator, that is, a resonator with more than one section. On the basis of that discussion, we may simply lump Q_{optical}, the nonresonant part of Q_χ, with Q_U, the unloaded Q of the resonator and set $Q_\chi = Q_{\mathrm{EPR}}$. The quantity Q_{EPR} is the source of the EPR signal. Off of EPR resonance, Q_{EPR} is infinite because there is no absorption of the FIR field. On EPR resonance, Q_{EPR} is finite due to FIR absorption. An expression for Q_L that incorporates these effects is

$$\frac{1}{Q_L} = \left(\frac{1}{Q_U} + \frac{1}{Q_{\mathrm{optical}}}\right) + \left(\frac{1}{Q_{R_1}} + \frac{1}{Q_{R_2}}\right) + \frac{1}{Q_\chi} \tag{49}$$

where Q_{R_1} and Q_{R_2} model the coupling into and out of the resonator. We may write $1/Q_\chi = \eta\chi''$ in Eq. (49), where η is the filling factor of the resonator (subsequently derived) and χ'' is the absorptive part of FIR susceptibility.

Q_L, the loaded Q, is one of the parameters accessible to experimental measurement if the longitudinal mode number is known. Figure 3 shows a fixed frequency, variable mirror spacing scan. From the ratio of the spacing of the resonances to the width, we may define the resonator finesse $\mathcal{F} = L/\Delta L$, where L is the longitudinal mode spacing, which is approximately equal to $\lambda/2$, and ΔL is the mirror travel that corresponds to the power FWHM, which is approximately equal to $q\,\Delta\lambda/2$, where q is the longitudinal mode number (Earle, 1991; Goy, 1983). The field intensity in the resonator is proportional to the finesse, so that increasing the finesse for a given mirror spacing leads to a larger B_1. From knowledge of q and $\mathcal{F}$, we may conclude the loaded Q as $Q_L = q\mathcal{F}$. Our resonator has a $Q_L \approx 200$. In a conventional TE_{102} microwave cavity, $q = 1$ so that the Q of a conventional microwave cavity is equal to its finesse.

For an arbitrary Gaussian beam mode [cf. Eq. (130)] the Poynting vector $\mathbf{S} = \mathbf{E} \times \mathbf{H}^*/8\pi$ at the beam waist $(z = 0)$ may be used to calculate the B_1 field for a given beam waist w_0 as follows:

$$\begin{aligned} P &= c \int_\Sigma \mathbf{S} \cdot d\Sigma \\ &= \frac{cB_1^2}{8\pi} \int_0^{2\pi} \int_0^\infty d\varphi\, \rho\, d\rho\, x^l \left[L_p^l(x)\right]^2 e^{-x} \end{aligned}$$

$$= \frac{cw_0^2B_1^2}{16}\int_0^\infty x^l\left[L_p^l(x)\right]^2 e^{-x}\,dx$$

$$= \frac{cw_0^2B_1^2}{16}\,\frac{(l+p)!}{p!} \tag{50}$$

using Eq. (139) of the Appendix, where $x = 2\rho^2/w_0^2$. For the fundamental mode, $l = p = 0$ and the ratio of factorials is unity. If we take $P = 3$ mW and $w_0 = 6.7$ mm, then

$$B_1 = \frac{4}{w_0}\sqrt{\frac{P}{c}} \tag{51}$$

$$= 6\ \mathrm{mG} \tag{52}$$

We see that reducing the beam waist increases B_1. We note that B_1 is more weakly dependent on P. We will derive an expression for he B_1 field at the sample in a Fabry–Pérot resonator in Section VIII after we have developed the appropriate lumped equivalent circuit for a transmission mode spectrometer.

In the presence of a sample, the fields and the Q_L of the resonator will change. It is possible to account for this effect by calculating the filling factor of the sample-loded resonator. We will defer explicit calculation of the filling factor until we have addressed the role played by the sample dimensions.

The dimensions of the sample are important in determining the performance of the spectrometer because the sample can extend over several wavelengths in several dimensions, at least in principle, which enhances interferometric effects within the sample. Neglecting losses in the sample for the moment, we note that if the sample is an integral number of half-wavelengths thick, it functions like a Fabry–Pérot. In order to understand this, we will sketch a derivation that takes into account the index of refraction of the dielectric material and reflection from the sample–air interfaces. First, note that the optical phase difference across the sample is nkt, where n is the index of refraction and t is the thickness. The resonance condition for such a slab is given by Eq. (44) with kt replaced by nkt, namely,

$$nkt - (2p + l + l)\tan^{-1}(t/z_0) = q\pi \tag{53}$$

If $t \ll z_0$, which is a case of practical interest, we may approximate the resonance condition as $nkt \approx q\pi$. The minimum reflected power is zero on resonance, regardless of the surface reflectivity, and all of the power is transmitted. This is an example of what optical engineers call an absentee layer. There is also a transmission line analogy to the present case. A half-wavelength section of characteristic impedance Z_1 in a transmission line with characteristic impedance Z_0 has a reflection coefficient of zero.

Due to the finite beam growth of a Gaussian beam, there will be a phase error that causes the surface reflectivities to be slightly different for the two surfaces. The response of a Fabry–Pérot resonator with surfaces of different reflectivities is given in Section X, where we show that the minimum reflected power differs slightly from zero for surfaces with slightly different reflectivities.

In any practical system, there will be at least three layers arranged as follows: sample holder, sample, sample holder. If the sample and sample holder layers are an integral number of half-wavelengths thick, we may think of the ensemble as a set of three absentee layers in series and the calcultion carries through as before. These qualitative arguments are put on a firmer footing in Section X, where we calculate the transmission and reflection coefficients for a compound Fabry–Pérot resonator with more than two reflecting surfaces.

Until now we have confined our attention to samples with low losses. In a resonator of high fenesse, the presence of absorption not only broadens the resonator response, it also reduces the transmitted power. The optimum solution for studying lossy samples is to place them in regions of low **E** field in the resonator. We know that the mirrors of the resonator are nodes of the **E** field because the tangential **E** field must vanish at the surface of a good conductor. For aqueous samples, one can use a modification of the method used previously. If the thickness of the sample and sample holder is less than $\lambda/4$, then multiple beam interference effects are negligible and we may regard the lossy medium simply as a thin film on the mirror. Hence, one should construct as aqueous sample holder as follows: thin film, sample, thin film, where the thickness of each layer is $\lambda/10$ or less. We have successfully implemented these concepts for aqueous and other lossy samples, and they are discussed further elsewhere (Barnes and Freed. 1996).

It is intuitively obvious that thin samples will reduce the filling factor of the resonator. We will show subsequently how to calculate the filling factor in simple cases. If more spins are needed to see a signal, we can use two thin layer samples separated by a low-loss dielectric spacer an integral number of half-wavelengths thick. This arrangement is equivalent to a Fabry–Pérot resonator that consists of a dielectric with highly reflective surfaces, which is discussed in Section X (the layout of such a scheme is shown in Fig. 9). We choose the position of such a sample such that the high-loss medium is always in a region of low **E** field. This "sandwich" approach relies on knowledge of the index of refraction of the spacer material. If the spacer thickness is chosen carefully, the absentee layer argument that we previously outlined should go through unmodified.

Until now we have only addressed the thickness of the sample. By proper choice of the sample dimensions, it is only the thickness of the sample along the optical axis that matters in calculating the resonator filling factor. The beam waist in the resonator is usually chosen to be small in order to enhance the B_1 field at the sample. The Cornell 250-GHz transmission spectrometer uses a beam waist of 2.2 mm in the resonator. From the criteria we have derived so far, this would imply that a sample of radial extent greater than 8.8 mm will not distort the fields of the resonator. There is no advantage to increasing the radial extent of the sample over this value because the B_1 field is exponentially decreasing away from the optical axis. The only way to increase the number of spins that are excited by the fields in the resonator is to increase the sample thickness. For low-loss samples, rather large filling factors approaching unity can be obtained.

The most straightforward way to calculate the filling factor is to calculate the ratio of electromagnetic energy stored in the sample to the electromagnetic energy stored in the resonantor. Then we may use the result that the total energy in the resonator, which represents the sum of the dielectric and air regions, is

$$E_{\text{total}} = (1/8\pi)E_0^2 w_0^2(t\Delta + d) \tag{54}$$

where E_0 is the field strength in the resonator and Δ is a quasioptical correction to the thickness given by (Yu and Cullen, 1982)

$$\Delta = n^2/\left[n^2\cos^2(nkt - \Phi_T) + \sin^2(nkt - \Phi_T)\right] \tag{55}$$

where Φ_T is a small phase correction that is 2 orders of magnitude smaller than nkt for thin or very thick ($t \approx d$) samples (Yu and Cullen, 1982), which are the two cases of greatest experimental interest. We will neglect Φ_T in the sequel.

The filling factor may be written now by inspection,

$$\eta = t\Delta/(t\Delta + d) \tag{56}$$

For those samples that have a radius greater than twice the beam radius over the entire sample, the sample radius does not enter the filling factor calculation because it has no effect on the fields.

VII. Transmission Mode Resonator

The resonator problems that we have discussed are of limited interest until we couple to a source and load in order to examine the response of

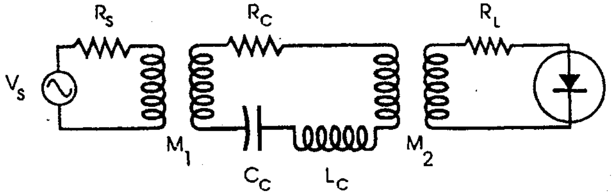

FIG. 6. Lumped equivalent circuit for a transmission mode spectrometer near a resonance. V_S is the output voltage of the millimeter wave source, R_S is the source resistance, L_C and C_C are the equivalent inductance and capacitance of the resonator, R_C is the resonator resistance, and R_L is the load resistance of the detector. The mutual inductances M_1 and M_2 model the coupling into and out of the resonator.

the resonator. In Section V, we found it helpful to model a quasioptical system as a transmission line, where the beam waist plays the role of the characteristic impedance, in order to understand the results of the beam-waist transformation calculation. Here, we will model the spectrometer by an equivalent circuit in order to gain insight into the factors that influence spectrometer performance when we vary the coupling into and out of the resonator.

We may subsume all of the complexity of the full electromagnetic wave description of the Gaussian beam and its coupling to various elements of the resonator into two phenomenological constants: the mutual inductances M_1 and M_2 of Fig. 6. This procedure is equivalent to that used to model variable iris coupling into a waveguide cavity, for example.

Once we have an equivalent circuit, we may manipulate the circuit equations to explore the effect on spectrometer performance of changing the values of circuit elements. It would be useful to have a variable coupling scheme in order to tune the spectrometer for optimum performance, just as in the microwave spectrometer case. Such a scheme is described in Section X.

We may write a lumped equivalent circuit for the resonator and coupled transmission lines following the prescription in RLS-8 (Montgomery *et al.*, 1948) as shown in Fig. 6. At resonance, the power P_L into the load resistance R_L is found from

$$P_L = \frac{4\beta_1\beta_2 P_0}{(1 + \beta_1 + \beta_2)^2} \tag{57}$$

where $P_0 = V_S^2/4R_S$. The quantities β_1 and β_2 are the coupling parameters to the resonator, and they take the values

$$\beta_1 = \frac{\omega^2 M_1^2}{R_S R_C} \equiv \frac{Q_U}{Q_{R_1}} \tag{58}$$

$$\beta_2 = \frac{\omega^2 M_2^2}{R_L R_C} \equiv \frac{Q_U}{Q_{R_2}} \tag{59}$$

where it is assumed that R_S and R_L have been matched to a transmission line of characteristic impedance Z_0. The βs give the radiation Qs directly if the unloaded Q is unknown. We may define a transmission loss function $T(\omega_0) = P_L/P_0$, which gives, for the optimal coupling case, $\beta_1 = \beta_2 = 1/2$, $T_{\text{opt}}(\omega_0) = 1/4$, or -6 dB. The optimal coupling case also corresponds to an unloaded Q, $Q_U = 2Q_L$, as one may see from the formula for Q_L:

$$\frac{1}{Q_L} = \frac{1}{Q_U} + \frac{1}{Q_{R_1}} + \frac{1}{Q_{R_2}} \tag{60}$$

$$Q_U = Q_L(1 + \beta_1 + \beta_2) \tag{61}$$

If we measure the power incident on the detector, therefore, we can estimate β from the expression for the transmission loss assuming that the couplings are the same. Using the estimate of β, we can then calculate the unloaded Q from a measurement of the loaded Q.

The quantity Q_U may be written in terms of the circuit parameters of Fig. 5 as $Q_U = \omega L/R_C$. The inductance of the cavity may be found by calculating the flux passing through a strip normal to the E field and the optical axis in the resonator of width $\lambda/2$, multiplying by the mode number q, and dividing by the current flowing in the cavity $i_c = (V_S/R_S)\sqrt{(\beta_1)}/(1 + \beta_1 + \beta_2)$. Crudely speaking, the magnetic energy stored in the resonator may be found from the energy stored per mode $(w_0^2 B_1^2/16)(\lambda/2)$ times the mode number q. The peak power stored in the resonator is then

$$P_{\text{stored}} = \frac{c\overline{w}_0^2 \overline{B}_1^2}{16} q \tag{62}$$

where $\overline{B}_1$ is the average peak FIR magnetic field in the resonator and $\overline{w}_0^2$ is the average waist radius in the resonator. We may calculate $\overline{w}_0^2$ from Eq. (20) as

$$\begin{aligned}\overline{w}_0^2 &= w_0^2\left(\frac{z_0}{d}\right)\int_0^{d/z_0}\left[1 + (x)^2\right] dx \\ &= w_0^2\left[1 + \frac{1}{3}\left(\frac{d}{z_0}\right)^2\right] \\ &\approx \frac{4}{3} w_0^2\end{aligned} \tag{63}$$

for d approximately equal to the confocal separation. In terms of the observed finesse, we may write

$$Q_U = q\mathcal{F}(1 + \beta_1 + \beta_2) \tag{64}$$

Our spectrometer has a measured $T(\omega_0) = -23$ dB, from which one may infer a $\beta = 0.038$ and $Q_U \approx Q_L$. (See Earle *et al.* (1996b) for a more complete discussion.) Such a high value of transmission loss also has been measured for other millimeter band waveguide-coupled resonators (Goy, 1983). In Section XI, we discuss methods for lowering the transmission loss by dispensing completely with waveguide coupling. The loaded Q is approximately 200, which implies that the unloaded Q of the resonator in the presence of a large sample is also approximately 200, that is, $\eta Q_L \approx Q_U$. The measurement does not correct for the perturbing effect of the chopper on the fields within the quasioptics, however, We must therefore regard the β values as suggestive, not definitive. The principal advantage of such low coupling parameters is that Q_L is not particularly sensitive to cavity drift. In fact, we are able to collect spectra over a broad temperature range without retuning the resonator. Working at low temperatures does require more frequent tuning, however. Nevertheless, it is still possible to collect low-temperature spectra for approximately a half hour without retuning.

Variable coupling, as discussed in Section X, would allow us to optimize the coupling for each sample. We will examine the effect of variable coupling on the sensitivity and the B_1 at the sample in Sections VIII and XI.

VIII. Spectrometer Sensitivity

The expression for the resonator Q in the presence of a sample may be found by defining the sample quality factor as the ratio of energy stored in the cavity to energy dissipated in the sample due to EPR absorption, which may be related to the filling factor η and the rf susceptibility χ'', namely,

$Q_\chi = 1/\eta\chi''$. Recall that we have combined the nonresonant contribution to the sample Q with Q_U. The expression for the loaded Q then may be modified as

$$\frac{1}{Q_L} = \frac{1}{Q_U} + \frac{1}{Q_{R_1}} + \frac{1}{Q_{R_2}} + \frac{1}{Q_\chi} \tag{65}$$

Dielectric losses also may be combined with Q_U. We will show in the sequel that the spectrometer sensitivity depends on the fractional change in the loaded Q as the sample goes into and out of resonance, whence one may readily write

$$\frac{\Delta Q_L}{Q_L} = \frac{(Q_L)\chi''\eta}{1 + (Q_L)\chi''\eta} \tag{66}$$

The change in rf voltage at the detector due to a change in the loaded Q may be calculated easily from the equivalent lumped circuit for the resonator, where the resonance absorption may be modeled as a small series resistance δR. The detector voltage is

$$\frac{V_L}{\sqrt{R_L}} = \frac{2\sqrt{P_0}\,\sqrt{(\omega^2 M_1)(\omega^2 M_2)/R_S R_L}}{\omega^2 M_1/R_S + R_C + \delta R + \omega^2 M_2/R_L} \tag{67}$$

where P_0 is the available power of the FIR source $(V_S^2/4R_S)$. We may now easily derive the change in the detector voltage (for small δR): $\Delta V_L/V_L = \Delta Q_L/Q_L$. Inserting the expression for the change in Q due to resonance absorption, we find

$$\frac{\Delta V_L}{\sqrt{R_L}} = \frac{V_L}{\sqrt{R_L}}(Q_L)\chi''\eta \tag{68}$$

using Eq. (66), where we assume $\eta\chi'' \ll 1$.

The sensitivity limit corresponds to a signal-to-noise ratio of 1 : 1, which may be modeled by assuming a Johnson noise source at T_d of resistance R_L, where T_d may be calculated from the noise equivalent power of the detector, assuming that T_d has a $1/f_{\text{mod}}$ modulation frequency dependence. For a modulation frequency of 100 kHz, we measure $T_d \approx 10^7$ K. This should be compared to X-band detectors, which typically (Abragam and Bleaney, 1970, pp. 125–132) have a noise temperature $\approx 10^3$ K. FIR homodyne detectors are intrinsically noisier than their microwave frequency counterparts. Equating the Nyquist expression for the Johnson noise in a bandwidth Δf to the change in voltage at the detector due to the resonance absorption leads to the following expression for the

minimum observable rf susceptibility:

$$\chi''_{\text{min}} = \frac{1}{\eta Q_L}\,\frac{(1+\beta_1+\beta_2)}{\sqrt{\beta_1\beta_2}}\left(\frac{k_B T_D\,\Delta f}{P_0}\right)^{1/2} \tag{69}$$

where it is assumed that the detector is the dominant noise source in the spectrometer. If we choose optimal coupling $\beta_1 = \beta_2 = 1/2$, then the expression for χ''_{min} becomes

$$\chi''_{\text{min}} = \frac{4}{\eta Q_L}\left(\frac{k_B T_d\,\Delta f}{P_G}\right)^{1/2} \tag{70}$$

For lines that are not too broad (Abragam and Bleaney, 1970, p. 126), we may approximate $\chi'' \approx \chi_0(\omega/\Delta\omega)$, where χ_0 is the static susceptibility, ω is the Larmor frequency, and $\Delta\omega$ is the linewidth. In this regime, therefore, we may write

$$\chi_0^{\text{min}} = \frac{\Delta\omega}{\omega}\,\frac{1}{\eta Q_L}\,\frac{(1+\beta_1+\beta_2)}{\sqrt{\beta_1\beta_2}}\left(\frac{k_B T_D\,\Delta f}{P_0}\right)^{1/2} \tag{71}$$

If, in addition to the foregoing assumptions, we may use the Curie expression for the static susceptibility, then we may calculate the minimum observable number of spins

$$N_{\text{min}} = \frac{3V_S k_B T_S}{g^2\beta_e^2 S(S+1)}\,\frac{\Delta\omega}{\omega}\,\frac{1}{\eta Q_L}\,\frac{(1+\beta_1+\beta_2)}{\sqrt{\beta_1\beta_2}}\left(\frac{k_B T_D\,\Delta f}{P_0}\right)^{1/2} \tag{72}$$

where V_S is the sample volume and T_S is the sample temperature.

One may include the effect of the modulation amplitude on the minimum detectable number of spins, for modulation amplitudes less than the linewidth, by multiplying the expression for N_{min} by a factor (Poole, 1967) $\Delta H_{\text{pp}}/H_{\text{mod}}$.

Finally, we may normalize by the multiplicity of the hyperfine lines in nitroxides by multiplying N_{min} by $2S + 1$. Putting all the pieces together, we have an expression that may be compared to experiment, namely,

$$N_{\text{min}} = \frac{3V_S k_B T_S(2S+1)}{g^2\beta_e^2 S(S+1)}\,\frac{\Delta H_{\text{pp}}}{H_0}\,\frac{\Delta H_{\text{pp}}}{H_{\text{mod}}} \times \frac{1}{\eta Q_L}\,\frac{(1+\beta_1+\beta_2)}{\sqrt{\beta_1\beta_2}}\left(\frac{k_B T_D\,\Delta f}{P_0}\right)^{1/2} \tag{73}$$

Assuming a $g = 2$ system with a 1-G linewidth at 8.9 T using a 0.5-mM sample near room temperature, a large filling factor $\eta \approx 1$, a sample volume approximately 0.5 cm^3, $Q_L \approx 200$, a modulation amplitude $\approx \Delta H_{pp}/10$, coupling factors $\beta = \beta_1 = \beta_2 = 0.04$, a noise temperature $T_d \approx 10^7$ K for λ Schottky detector, a postdetection bandwidth of 1 Hz, and an FIR power of 3 mW leads to $N_{\min} \approx 10^{10}$. This value corresponds to a motionally narrowed nitroxide spin probe in a low-loss solvent. The experimentally observed $N_{\min}^{(\mathrm{obs})} \approx 10^{11}$. Given the uncertainties in the various parameters as well as the neglect of the noise figure contribution from the postdetection chain, the agreement is satisfactory. Using optimum coupling will reduce $N_{\min}$ by a factor $4\sqrt{\beta_1 \beta_2}/(1 + \beta_1 + \beta_2)$. If we take $\beta_1 = \beta_2 = \beta = 0.04$, then $N_{\min}^{(\mathrm{opt})} \approx 2 \times 10^9$. Increasing the Q_L by a factor of 10 will reduce $N_{\min}^{(\mathrm{opt})} \approx 2 \times 10^8$, which compares with the expression for the optimum sensitivity of a Fabry–Pérot resonator in the FIR (Lebedev, 1990). If we assume that the same scaling obtains for the observed $N_{\min}$, $N_{\min}^{(\mathrm{obs})}$, then for an optimally coupled resonator with $Q_L = 2000$, we predict $N_{\min}^{(\mathrm{obs})} \approx 2 \times 10^9$, with all other parameters fixed, which is comparable to $N_{\min}^{(\mathrm{obs})}$ at 150 GHz for a Fabry–Pérot resonator (Lebedev, 1990): $N_{\min}^{(\mathrm{obs})}$ (150 GHz) $= 2 \times 10^9$. In our experience, use of an InSb bolometer detector will reduce these values of $N_{\min}$ by about a factor of 4.

From Eq. (73) it is clear that there are other ways to reduce $N_{\min}$. One can work at higher powers, at least until saturation occurs, or use a detector with lower noise temperature or both. Before purchasing a higher power source, one should check carefully to ensure that the detector performance is not limited by higher power levels. Schneider (1982) discusses the performance of millimeter wave diodes in detail.

A large background power, which is an ineluctable consequence of the transmission mode, can dramatically reduce the sensitivity of diodes operated as detectors. The signal current I_S that flows in the detector is given by (Schneider, 1982)

$$I_S = \beta P_{\mathrm{rf}} \tag{74}$$

$$\beta = \frac{e}{2nk_BT}\left(1 + \frac{R_S}{R_B}\right)\left\{1 + \left(\frac{f}{f_C}\right)\right\}^{-1} \tag{75}$$

$$R_B = \frac{nk_BT}{e(I_0 + I_S)} \tag{76}$$

$$R_V = R_B + R_S \tag{77}$$

where P_{rf} is the power incident on the detector, β is the current responsivity of the diode, which is typically 1 μA/μW, e is the elementary charge of the electron, n is the ideality factor of the diode, which is close to unity in a good design, k_B is Boltzmann's constant, T is the temperature of the diode, R_S is the spreading resistance of the diode, which is typically 5 Ω, R_B is the base-band dynamic resistance, which is typically 5000 Ω for incident powers up to a few microwatts, f is the frequency of the incident power, f_C is the cutoff frequency of the diode, which is approximately 1 THz for near-millimeter diodes, and I_0 is the dc bias current, which is typically on the order of a few microamperes.

The figure of merit for a millimeter diode operated as a detector is the video resistance R_V, which in turn depends on R_B, which has a significant power dependence for high incident powers through its dependence on I_S. The current responsivity β is only weakly dependent on the incident power, and we will take it be 1 μA/μW for this analysis. For an incident power of 1 mW, Eq. (74) implies $I_S = 1$ mA, and we may use Eq. (76) to show $R_B = 25$ Ω. For an incident power of a few microwatts or lower, Eq. (76) shows that R_B is essentially independent of input power and equal to 5000 Ω. Hence, high incident powers reduce the video resistance.

The minimum detectable signal for a detector is given by (Schneider, 1982)

$$P_{\mathrm{rf,\,min}} = \frac{1}{\beta}\left(\frac{4k_BT\Delta f}{R_V}\right)^{1/2} \tag{78}$$

where Δf is the receiver bandwidth at the signal band, which is approximately 100 GHz for the WR-4 waveguide used in the fore-optics before the detector diode. Equation (78) may be rewritten to estimate the ratio of minimum detectable powers for high and low background powers at the same receiver bandwidth $P_{\mathrm{rf,\,min}}^{\mathrm{opt}} = P_{\mathrm{rf,\,min}}(25\ \Omega/\ 5000\ \Omega)^{1/2}$, which translates into a reduction of $P_{\mathrm{rf,\,min}}$ by a factor of 16 if we optimize the incident power on the detector.

We choose our cavity coupling $\beta \approx 0.04$ to limit the incident power on the detector and thereby maintain its sensitivity. The price we pay is reduced B_1 at the sample as we subsequently will show. The most practical way to maintain high sensitivity without sacrificing source power is to work in reflection mode. A well matched resonator will have a reflected power of -30 dBc or lower, which corresponds to power levels of 1 μW or lower for a source power of 0 dBm (1 mW).

We discuss in Section IX techniques for constructing a reflection mode spectrometer based on quasioptical techniques that will have a receiver input bandwidth $\Delta f = 25$ GHz. The quasioptical component that accomplishes this function is a Polarization Transforming Reflector (PTR) discussed in Howard *et al.* (1986) We use the PTR as a wave plate that rejects noise components outside of a narrow band. We discuss this point further in Section IX. Based on Eq. (78), this should allow a further reduction in $P_{\mathrm{rf,\,min}}$ by a factor of 2 compared to the current spectrometer. We may summarize the discussion as follows. A reflection mode spectrometer has an intrinsically lower background and noise input bandwidth than an optimally coupled transmission mode spectrometer. Based on the discussion after Eq. (78), the low background of a reflection mode translates into a factor of 16 reduction in N_{min} vis-à-vis an optimally coupled transmission mode spectrometer. Furthermore, reducing the bandwidth of the receiver from 100 to 25 GHz will reduce N_{min} by a factor $\sqrt{100\ \mathrm{GHz}/25\ \mathrm{GHz}} = 2$ [cf. Eq. (78)]. The total reduction in N_{min} will be a factor of 30 by combining the two effects, or $N_{\mathrm{min}}^{(\mathrm{th})} = 6 \times 10^6$ spins. This leads to a predicted *observable* $N_{\mathrm{min}}^{(\mathrm{obs})}$ of about 6×10^7 spins if we use the same scaling arguments as in the preceding text. (Again, use of an InSb bolometer should reduce these values of N_{min} by about a factor of 4.)

Let us now calculate the B_1 that we can achieve at the sample. We may use the equivalent lumped parameter circuit in Fig. 6 for this purpose. The power dissipated in the resonator may be written in terms of measurable quantities as

$$P_{\mathrm{diss}} = \frac{4P_0\beta_1}{(1+\beta_1+\beta_2)^2} \tag{79}$$

We have already calculated the power stored in the resonator in Eq. (62). If we define the unloaded Q as the ratio of power stored in the resonator to the power dissipated in the resonator, then we may express B_1 using Eqs. (62), (64), and (79) as follows:

$$P_{\mathrm{stored}} = Q_U P_{\mathrm{diss}}$$

$$\frac{c\bar{w}_0^2\bar{B}_1^2}{16} = 4P_0\mathcal{F}\frac{\beta_1}{1+\beta_1+\beta_2}$$

$$\bar{B}_1 = 8\sqrt{\frac{P_0\mathcal{F}}{c\bar{w}_0^2}\,\frac{\beta_1}{1+\beta_1+\beta_2}} \tag{80}$$

Some typical numbers are $P_0 = 3$ mW, $\mathcal{F} = 10$, $\bar{w}_0^2 = (4/3) \times (2.2\ \mathrm{mm})^2$, and $\beta_1 \approx 0.04$, from which we may derive $B_1 = 19.4$ mG. For the optimal coupling case $\beta_1 = \beta_2 = 0.5$, the optimum $B_1 = 52$ mG for fixed finesse, beam waist, and power.

In order to see if such a value of B_1 would cause spectral saturation, we may estimate the corotating component of the rf magnetization from the Bloch equations (Abragam and Bleaney, 1970, pp. 115–119), whence

$$\frac{\chi'' B_1}{M_0} = \frac{\gamma B_1 T_2}{1+\gamma^2 B_1^2 T_1 T_2} \tag{81}$$

which is maximized when $\gamma^2 B_1^2 T_1 T_2 = 1$. Under this condition, we may write an expression for the generator power required to maximize χ'' for a given T_1, namely,

$$P_0 = \frac{(1+\beta_1+\beta_2)c\bar{w}_0^2}{64\gamma^2\mathcal{F}\beta_1 T_2}\,\frac{1}{T_1} \tag{82}$$

If $P_0 = 3$ mW and we assume a linewidth of 1 G, then χ'' is a maximum for $T_1 \approx 4 \times 10^{-4}$ s. Since T_1s are usually shorter than this, spectral saturation should not be a problem. In the optimum coupling case $\beta_1 = \beta_2 = 0.5$, there will be no saturation for $P_G = 3$ mW if $T_1 < 5 \times 10^{-5}$ s.

IX. Reflection Mode Spectrometer

In this and the following sections, we will discuss a novel approach that will allow the spectrometer to be operated in the reflection mode, shown in Fig. 7. In Section VIII, we already calculated the expected gain in sensitivity from changing to the reflection mode. In this and the following sections, we will discuss the quasioptical components available to perform the required signal processing. Finally, we will present a design specification that allows us to demonstrate the advantages of quasioptical design techniques in a practical application. A broadband spectrometer based on these principles has been built and tested at 170 GHz. See Earle *et al.* (1996b) for more details.

In a reflection mode spectrometer of high finesse $\mathcal{F}$ or quality factor Q, the reflected power when matched on resonance is many decibels below the incident power, which reduces the noise floor by many decibels with respect to a transmission mode resonator. When the ESR sample is resonant, the residual resonator mismatch changes, which causes the reflected power to change, and a small signal on a low background is presented to the detector. In order for the signal to be detected, however, it must be discriminated from the radiation incident on the resonator, just as in a conventional reflection mode ESR spectrometer.

In optical terms, we need some means of transmit–receive duplexing. This is especially important for millimeter wave diodes, which may be burned out (Chester, 1988) if the incident power is above 0 dBm (1 mW) and for millimeter wave vacuum oscillators, which may be damaged by back-reflected power (Griffin, 1995). At conventional microwave frequencies, we may use ferrite circulators or a "magic" T in order to perform the duplexing. We present a new approach to the duplexing needs of ESR spectroscopists in the FIR by using polarization coding to perform the duplexing function. In order to code the radiation incident on and re-

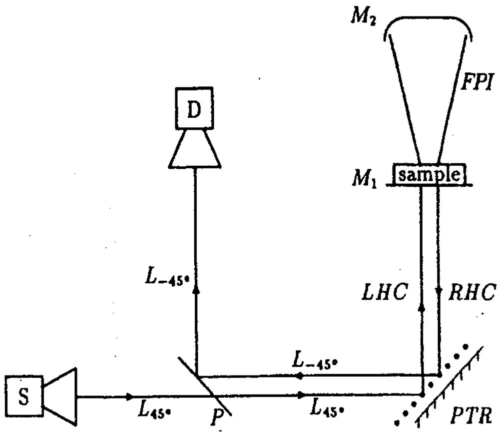

FIG. 7. Simplified optical layout for a reflection mode spectrometer with polarization coded duplexing. Polarizer P passes radiation linearly polarized at 45° ($L_{45°}$) with respect to the normal to the plane of the page. The polarization-transforming reflector PTR converts linearly polarized light to left-hand circularly (LHC) polarized light. Upon reflection from the Fabry–Pérot interferometer (FPI), the radiation is right-hand circularly (RHC) polarized. After the second pass through the PTR, the polarization vector is rotated by 90° with respect to the incident radiation $L_{-45°}$. This polarization state is reflected by polarizer P into the detector D. The diverging lines in the FPI indicate the presence of diffractive beam growth that is controlled by the curved mirror M_2. The reflectivity of M_1 may be varied to adjust the coupling into and out of the FPI as discussed in the text. A working implementation of this concept is described in detail by Earle *et al.* (1996b).

flected from the resonator, the polarization of the reflected power must be different from the incident power. If we use linearly polarized radiation at the resonator, polarization coding is impossible with passive, linear elements. In such a situation, we might use a power division interferometer, such as a Michelson interferometer, which uses a dielectric beam splitter as the millimeter wave equivalent of a "magic" T in order to separate the reflected power from the incident power. A simple amplitude division beam divisor does have a significant disadvantage, however, as we discuss further in the sequel.

Although all laboratories that perform high-field ESR have experimented with Fabry–Pérot resonators instead of fundamental mode microwave cavities, few laboratories have as yet explored quasioptical implementations of common microwave devices such as a "magic" T or circulator in an FIR-ESR spectrometer (see Earle and Freed, 1995; Earle *et al.* 1996b; Smith, 1995). Part of the problem is the unfamiliar appearance of optical circuits to spectroscopists who are only familiar with microwave circuits. One of the goals of this chapter is to acquaint the reader with the quasioptical synonyms of conventional microwave components.

At first sight, it may seem surprising that a Michelson interferometer may be thought of as a "magic" T. However, any microwave component fabricated from a waveguide has a quasioptical counterpart, as discussed in Martin and LeSurf (1978). For the purposes of duplexing, however, a Michelson interferometer may not be the best choice. A conventionally configured Michelson interferometer returns half of the signal and half of the power to the source. Loss of signal reduces the sensitivity of the device, and reflected power can reduce the lifetime of the source, unless one uses an isolator, which typically has a nonnegligible insertion loss.

The layout for a novel scheme that overcomes the limitations of a Michelson duplexer is shown in Figure 7. The most important element of the spectrometer in Fig. 7 is the polarization-transforming reflector (PTR), which functions as a quarter-wave plate in this configuration. We will defer a detailed discussion of PTRs for the moment and focus instead on its functionality. To that end, consider Fig. 8a, where we have "unfolded" the optical layout between the PTR and the Fabry–Pérot interferometer (FPI) in order to see the evolution of the electric field polarization more clearly.

The FPI and the PTR both are devices that operate in reflection as we have configured them, so we must pause a moment and consider the effect of reflection on an arbitrary polarization vector. At the surface of an ideal conductor, which is a good approximation for the near-millimeter band, the tangential electric field must vanish. We will use a coordinate system in which the z-axis is always in the plane of incidence of the radiation. The plane of incidence is defined as the plane that contains the direction of propagation of the radiation and the normal to the reflecting surface. Figure 8a shows how this convention works in practice. The z axis is always along the direction of propagation. We choose the y axis to be normal to the plane of incidence and always in the same half-space, regardless of the direction of propagation. Finally, the orientation of the x axis is chosen to be normal to the local y and z axes, such that the triad of vectors xyz always forms a right-handed system. This convention is consistent with that of LeSurf (1990), which is optimized for discussing polarization processing elements that operate in reflection. The notation of Earle (1994) and Hecht and Zajac (1979, pp. 268–270) is best suited for discussing polarization processing elements that operate in transmission, although any convention will do, as long as it is applied consistently.

Let us now trace the polarization evolution of a Gaussian beam as it traverses the optical system shown in Fig. 7. Polarizer P passes radiation linearly polarized at 45° ($L_{45°}$) with respect to the normal to the plane of the page. The polarization-transforming reflector (PTR) converts linearly

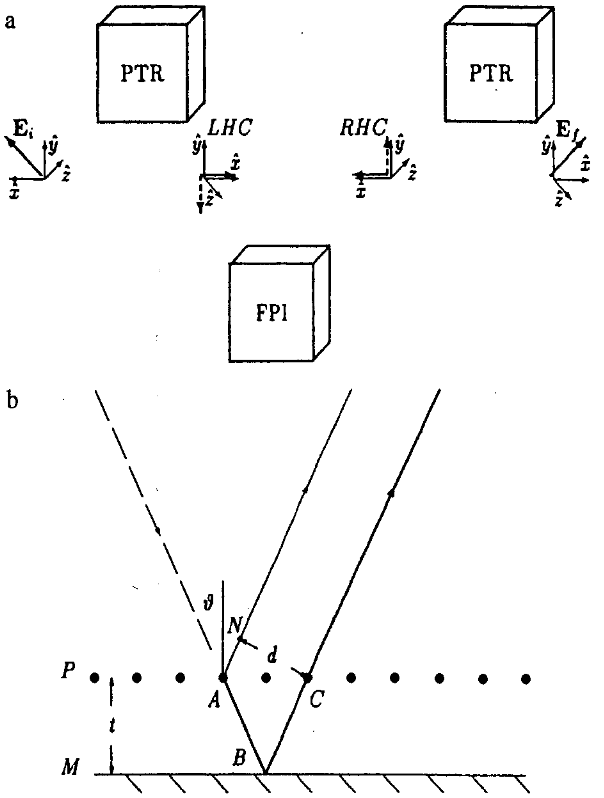

FIG. 8. (a) The polarization evolution of a Gaussian beam as it traverses a polarization-transforming reflector (PTR) and Fabry–Pérot interferometer (FPI) operating in reflection mode. Initially, the beam is linearly polarized at +45°. The exit beam is linearly polarized at −45°. The dotted lines indicate a polarization component that is retarded by a quarter period with respect to the polarization components indicated by a solid line. The optical layout shown here is an "unfolded" version of the polarization coding duplexer discussed in section IX. We have unfolded the layout in order to indicate more clearly how the polarization develops. In the physical realization of this device, the FPI reflects the Gaussian beam back toward the PTR, the optical path retraces itself, and the exit beam propagates antiparallel to the initial beam with a final linear polarization rotated by −90° with respect to the initial linear polarization. (b) The optical path difference and the beam separation between the reflected and transmitted portions of a Gaussian beam incident on a polarization-transforming reflector (PTR). The optical path difference $\Delta\mathscr{S} = AB + BC - AN$ is $2t\cos\vartheta$, where ϑ is the angle between the wave vector of the incident radiation and the normal to the plane of the PTR and t is the separation between the grid polarizer P and the mirror M. The geometrical phase difference $\vartheta = k\,\Delta\mathscr{S} = 4\pi t\cos\vartheta/\lambda$. We ignore contributions to φ from terms $\approx \Delta\mathscr{S}/z_0 \ll 1$, where z_0 is the confocal distance. The beam separation $d = 2t\sin\vartheta$. The dashed line indicates radiation linearly polarized at an angle of 45° with respect to the page surface. The thin solid line indicates radiation linearly polarized in the plane of the page and the thick solid line indicates radiation linearly polarized normal to the page. [From Earle *et al.* (1996b), by permission of the AIP.]

polarized light to left-hand circularly (LHC) polarized light. Upon reflection from the Fabry–Pérot interferometer (FPI), defined by mirrors M_1 and M_2, the radiation is right-hand circularly (RHC) polarized. The diverging lines in the FPI indicate the presence of diffractive beam growth that is controlled by the curved mirror M_2. After the second pass through the PTR, the polarization vector is rotated by 90° with respect to the incident radiation $L_{-45°}$. This polarization state is reflected by polarizer P into the detector D. The reflectivity of M_1 may be varied to adjust the coupling into and out of the FPI as discussed in subsequent text. From a "black box" point of view, we have passed linearly polarized light twice through a quarter wave plate, which has the same effect as a single passage through a half-wave plate, in order to rotate the linear polarization of the exit beam by $\pi/2$. The circularly polarized beam at the resonator is the most efficient way to exploit the available power from the mm wave source. The B_1 field at the sample is enhanced by a factor of $2^{1/2}$ compared to a linearly polarized beam. In the FIR, where source power is limited, this is an important consideration.

In this configuration, the duplexer also isolates the source from the deleterious effects of back-reflected power. Such a form of protection is crucial for high powered sources such as extended interaction oscillators (Wong, 1989) or backward wave oscillators. We see, then, that our polarization-coding techniques have a number of advantages over conventional methods of duplexing.

Another advantage of quasioptical duplexing over ferrite or waveguide technology is that polarizers and other processing optics can be made with very low losses and high power handling capability. For example, wire grid polarizers transmit cross-polarized radiation at levels of roughly −30 dB or lower (Goldsmith, 1982, p. 333) and have an insertion loss of 0.1 dB for the transmitted polarization. We see that polarization duplexing is very attractive in the near-millimeter band. Furthermore, ferrite- or waveguide-based components are not readily available above about 100 GHz.

Now that we have motivated the use of wave plates for duplexing via polarization coding, we may focus on a practical means of constructing a PTR. Figure 8b shows the optical layout of a practical, tunable PTR operating as a wave plate in the FIR. Such a PTR is described in detail in Howard *et al.* (1986). The phase shift between orthogonal linear polarization components at the output of the device is achieved by reflecting x-polarized light with polarizer P in Fig. 8 and allowing y-polarized light to acquire an optical path difference $\Delta\mathscr{S}$. Note that this leads to a beam separation d between the x and y components at the output of the device.

We will discuss the effect of a finite d on the performance of a PTR and discuss the conditions under which the beam separation may be neglected.

Figure 8b shows the optical path difference and the beam separation between the optical axes of the reflected and transmitted portions of a Gaussian beam. The optical path difference is

$$\begin{aligned}\Delta\mathcal{S} &= AB + BC - AN \\ &= 2t\cos\vartheta \qquad (83)\end{aligned}$$

where ϑ is the angle between the wave vector of the incident radiation and the normal to the plane of the PTR and t is the separation between the grid polarizer P and the mirror M. The geometrical phase difference is

$$\begin{aligned}\varphi &= k\,\Delta\mathcal{S} \\ &= 4\pi t\cos\vartheta/\lambda \qquad (84)\end{aligned}$$

We ignore contributions to φ from terms $\approx \Delta\mathcal{S}/z_0 \ll 1$, where z_0 is the confocal distance. The beam separation is

$$d = 2t\sin\vartheta \qquad (85)$$

In order to proceed beyond a qualitative description of how a PTR operates, it is convenient to use a mathematical description of coherent polarization states, which are a good approximation to the output of solid-state near-millimeter sources. The Jones vector formalism is well known (Hecht and Zajac, 1979, pp. 268–270; LeSurf, 1990) and well suited to the present purpose. Any transverse polarization vector can be represented by an equation of the form $\mathbf{E} = (E_H\hat{H} + E_v\hat{V})$, where $\hat{H}$ and $\hat{V}$ are the basis vectors of horizontal and vertical polarization, respectively. Note that E_H and E_V may be complex, which is useful for describing circular polarization. In particular, $\mathbf{E}_\pm = E_0(\hat{H} \pm i\hat{V})$, where the plus (+) indicates positive helicity and the minus (−) indicates negative helicity.

A Jones vector is a matrix representation of $\mathbf{E}$, namely,

$$\mathbf{E} = \begin{bmatrix} E_V \\ E_H \end{bmatrix} \qquad (86)$$

The Jones vectors of a horizontally polarized Gaussian beam $\mathbf{E}_H$ and a vertically polarized Gaussian beam $\mathbf{E}_V$ of field strength E_0 at the beam waist may be represented as

$$\mathbf{E}_V = E_0\begin{bmatrix} 1 \\ 0 \end{bmatrix}\exp\left(-\frac{\rho^2}{w_0^2}\right) \qquad (87)$$

$$\mathbf{E}_H = E_0\begin{bmatrix} 0 \\ 1 \end{bmatrix}\exp\left(-\frac{\rho^2}{w_0^2}\right) \qquad (88)$$

where w_0 is the beam-waist radius. In terms of the previously used coordinate system, $|\mathbf{E}_V| = E_y$ and $|\mathbf{E}_H| = E_x$.

In Section V we used the system transfer matrix to study the effect of an optical system on the parameters of a Gaussian beam. A similar formalism exists for studying the polarization evolution of a Jones vector as a beam traverses a polarization-transforming system. In this case the system transfer matrix is called a Jones matrix. The simplest Jones matrix is the matrix that describes the polarization vector reflected from an ideal mirror. In order to satisfy the boundary conditions of vanishing tangential E, we need a matrix with the property $\mathcal{M}\mathbf{E} = \begin{bmatrix} -E_V \\ E_H \end{bmatrix}$. The following Jones matrix has the desired behavior:

$$\mathcal{M} = \begin{bmatrix} -1 & 0 \\ 0 & 1 \end{bmatrix} \qquad (89)$$

A grid polarizer is the next object we need to consider. First we will define the Jones vectors for linear polarization at ±45° with respect to the y axis. These cases correspond to the situation shown in Fig. 8a. The required Jones vectors are

$$\mathbf{E}_{45} = \frac{E_0}{\sqrt{2}}\begin{pmatrix} 1 \\ 1 \end{pmatrix}$$

$$\mathbf{E}_{-45} = \frac{E_0}{\sqrt{2}}\begin{pmatrix} -1 \\ 1 \end{pmatrix}$$

A grid polarizer with the grid lines at a given angle φ with respect to the y axis will reflect radiation that is linearly polarized along the grid lines. If the grid lines make a ±45° angle with respect to the y axis, we need Jones matrices with the following behavior:

$$\begin{aligned}\mathcal{G}(45)E_{45} &= -E_{-45} \\ \mathcal{G}(45)E_{-45} &= 0 \\ \mathcal{G}(-45)E_{45} &= 0 \\ \mathcal{G}(-45)E_{-45} &= -E_{45}\end{aligned}$$

A Jones matrix that has this behavior is

$$\mathcal{G}(\pm 45) = \begin{pmatrix} -1/2 & \mp 1/2 \\ \pm 1/2 & 1/2 \end{pmatrix} \qquad (90)$$

We will not derive the form of $\mathcal{G}$ for an arbitrary inclination angle of the grid wires. We may verify that Eq. (90) is a special case of the following general relation (LeSurf, 1990) for arbitrary grid orientation angle ϑ:

$$\mathscr{G}(\vartheta) = \begin{pmatrix} -\cos^2\vartheta & -\cos\vartheta\sin\vartheta \\ \cos\vartheta\sin\vartheta & \sin^2\vartheta \end{pmatrix} \tag{91}$$

It is important to note that the preferred orientation of the grid for nonnormal incidence is with the grid in the plane of incidence of the Gaussian beam (Erickson, 1987). This corresponds to $\vartheta = 90°$. For this orientation of the grid, nonidealities due to cross-polarized components are minimized. The field transmitted by the polarizer is described by the complement of the Jones matrix of the polarizer, namely, $\mathscr{G}_T(\vartheta)$, which has the functional form (LeSurf, 1990)

$$\mathscr{G}_T(\vartheta) = \begin{pmatrix} \sin^2\vartheta & -\cos\vartheta\sin\vartheta \\ -\cos\vartheta\sin\vartheta & \cos^2\vartheta \end{pmatrix} \tag{92}$$

The PTR shown in Fig. 8 can be analyzed along the lines indicated in Howard *et al.* (1986). In our notation, we may use the Jones matrices of a polarizer $\mathscr{G}$, its complement $\mathscr{G}_T$, and a mirror $\mathscr{M}$ to express $\mathbf{E}_r$, the output beam of a PTR at the grid surface (where we may choose the beam radius $w \approx w_0$), namely,

$$\begin{aligned} \mathbf{E}_t = \Big[&\mathscr{G}(\vartheta)\exp(-\rho^2/w_0^2) \\ &+\mathscr{M}\mathscr{G}_T(\vartheta)\exp(-i\varphi)\exp\big(-(\boldsymbol{\rho} - \mathbf{d})^2/w_0^2\big)\Big]\mathbf{E}_i \end{aligned} \tag{93}$$

where $e^{-i\varphi}$ is a factor due to the phase shift of the transmitted portion of the incident beam, $\mathbf{E}_i$ is the Jones vector of the incident radiation, φ is given by Eq. (84), and $\mathbf{d}$ is the displacement vector of the transmitted beam along the x axis of the reflected beam whose magnitude is given by Eq. (85). We explicitly include the exponential factors $\exp(-\rho^2/w_0^2)$ and $\exp(-(\boldsymbol{\rho} - \mathbf{d})^2/w_0^2)$ in order to discuss the effects of beam displacement on the performance of the PTR.

The ideal response of the PTR, $\mathscr{P}(\vartheta, \varphi)$, in the absence of beam displacement effects, that is, $w_0 \to \infty$, may be written in Jones matrix form as

$$\mathscr{P}(\vartheta, \varphi) = \mathscr{G}(\vartheta) + \mathscr{M}\mathscr{G}_T(\vartheta)e^{-i\varphi} \tag{94}$$

The deviation of the practical device from the ideal response depends on the ratio d/w_0. We will perform an analysis of Eq. (93) that will allow us to estimate the bandwidth of the PTR. In particular, we will investigate the influence of phase and amplitude errors on the achievable level of performance. A high Q resonator will probably be the bandwidth-limiting component in a practical resonator. Nevertheless, it is an important exercise to verify that the bandwidth of the resonator falls within the bandwidth of the PTR.

The second term on the right-hand side of Eq. (93) may be expanded in terms of the Gaussian beam modes discussed in the Appendix. The vector $\mathbf{d}$ in Eq. (93) represents a displacement of a fundamental Gaussian beam along the $\varphi = 0$ or x axis. The beam radius w [cf. Eq. (20)] and radius of curvature R [cf. Eq. (21)] at the output of the PTR are nearly identical for the two components of the output beam because the path difference $\Delta\mathscr{S} \ll z_0$, where z_0 is the confocal length. Near the beam waist, $R \to \infty$ and so we neglect a phase correction in Eq. (93) that is proportional to $ik/2R$. We include the phase correction in the subsequent analysis for completeness, although its effect is small.

The phase and amplitude of a fundamental Gaussian beam shifted along the $\varphi = 0$ axis by a displacement $\mathbf{d}$ at the beam waist may be written by replacing ρ^2 with $(\boldsymbol{\rho} - \mathbf{d})^2$ in Eq. (130) and setting $p = l = 0$. We may approximate the phase and amplitude errors at the beam waist of such a beam as

$$\begin{aligned} &\exp\left(-(\boldsymbol{\rho} - \mathbf{d})^2\left(\frac{1}{w^2} + \frac{ik}{2R}\right)\right) \\ &\quad\approx \exp\left(-(\rho^2 + d^2)\left(\frac{1}{\omega^2} + \frac{ik}{2R}\right)\right) \\ &\qquad\times\left\{1 + \frac{2\rho d\cos\varphi}{w^2}\left(1 + i\frac{kw^2}{2R}\right) + \cdots\right\} \end{aligned} \tag{95}$$

This is an expansion in powers of d/w. We have stopped at the linear term because we expect the higher order terms to be small. Using the beam modes described by Eq. (130), we may write a mode decomposition of Eq. (95) as

$$\begin{aligned} &\exp\left(-(\rho - d)^2\left(\frac{1}{w^2} + \frac{ik}{2R}\right)\right) \\ &\quad\approx \exp\left(-\frac{d^2}{w^2}\right)\left\{u_{00} + \frac{d}{w}\left(1 + i\frac{kw^2}{2R}\right)\mathscr{R}\left[\sqrt{2}u_{11} - \frac{\sqrt{2}}{3}u_{21}\right]\right\} \end{aligned} \tag{96}$$

where the function u_{pl} is a Gaussian beam mode with radial mode number p and azimuthal mode number l given by Eq. (130).

With an angle of incidence of 30° and a beam waist $w = 6\lambda$, it is possible to achieve $d/w \approx 0.02$ for a quarter-wave plate, which we will take as a practical specification. The portion of the phase-shifted beam in the fundamental mode of Eq. (96) may be used to calculate the polarization purity of the PTR output beam. We therefore approximate

$$\mathbf{E}_r \approx u_{00}\left(\hat{x} + i\exp\left(-\frac{d^2}{w^2}\right)\hat{y}\right)$$
$$= u_{00}\left(P_+(\hat{x} + i\hat{y}) + P_-(\hat{x} - i\hat{y})\right) \tag{97}$$

where P_+ is the fraction of $\mathbf{E}_r$ that has positive helicity, P_- is the fraction of $\mathbf{E}_r$ that has negative helicity, and

$$\frac{P_-}{P_+} = \tanh\left(\frac{d^2}{2w^2}\right) \tag{98}$$

which gives $20\log_{10}(P_-/P_+) \approx -70$ dB for $d/w = 0.02$. The error terms in u_{11} and u_{21} are essentially a power loss term and may be approximated $P_{\text{loss}} \approx 20\log_{10}(d/w) = -34$ dB. This calculation shows that it is practical to build a PTR that has an extremely pure polarization response and very low losses to higher order modes.

In order to calculate the bandwidth of the PTR, we need to calculate the phase error introduced in the phase-shifted portion of the output beam as λ varies. For a PTR operated as a quarter-wave plate, we write

$$e^{ik\Delta\mathscr{S}} \approx i\left(1 - i\frac{\Delta\lambda}{\lambda_0}\right) \tag{99}$$

which states that for small phase errors, there is a portion of the output beam that is in quadrature with the desired phase shift. As $\Delta\lambda \to 0$, the phase error vanishes and the output beam is purely circularly polarized in the absence of amplitude errors.

We may study the effect of phase errors on the polarization purity of the fundamental by writing

$$u_{00}\left(\hat{x} + i\left(1 - i\frac{\Delta\lambda}{\lambda_0}\right)\hat{y}\right) = u_{00}\left[\Phi_+(\hat{x} + i\hat{y}) + \Phi_-(\hat{x} - i\hat{y})\right] \tag{100}$$

where $\Phi_+ = 1 - i\,\Delta\lambda/2\lambda_0$ is the amplitude of output radiation that has positive helicity and $\Phi_- = i\,\Delta\lambda/2\lambda_0$ is the amplitude of output radiation that has negative helicity. For $\Delta\lambda/\lambda_0 = 0.05$, which corresponds to a bandwidth of $\lambda_0 \pm 0.05\lambda_0$, the power ratio of negative helicity to positive helicity is $10\log_{10}|\Phi_+/\Phi_+|^2 = -32$ dB at the band edge. At 250 GHz, this corresponds to a bandwidth of 25 GHz, which is quite impressive for a tuned device.

We have shown now that the PTR is a device with excellent polarization purity over a broad frequency range and a low mode conversion loss. The measured performance of a PTR in the near-millimeter band when used as a half-wave plate is discussed by Howard *et al.* (1986). Our initial results (Earle *et al.*, 1996b; Tipikin *et al.*, 1996) are consistent with Howard's (1986) results. Nevertheless, we are working on improving the performance of our PTR further. The ultimate performance of the PTR depends on the ratio d/w, which may be optimized by using an angle of incidence as small as practical and a beam waist as large as possible. It is also important to ensure that the grid polarizer and flat mirror are parallel for optimum performance.

X. An Adjustable Finesse Fabry–Pérot Resonator

In order to optimize the performance of the resonator as samples of various sizes and loss tanagents are studied, it is useful to have a means to vary the loaded Q of the resonator. As we discussed in Section VIII, a poorly coupled resonator reduces the highest achievable signal-to-noise ratio.

One simple method for varying the coupling is to construct the resonator from two polarizers. We can show (Tudisco, 1988) that the finesse $\mathscr{F}$ of such a resonator is proportional to $\cos^2\vartheta$, where ϑ is the relative orientation of the two polarizers. This device is the quasioptical analog of the cavity coupling scheme of Lebedev (1990). There are several limitations to this scheme as pointed out by the author, namely, the radiation must be linearly polarized, which complicates transmit–receive duplexing in a reflection mode spectrometer; on resonance, the power minimum occurs in transmission, which precludes using the device in a reflection mode spectrometer if we wish to work with low background levels.

What we need is an optical device that has greater flexibility than a grid polarizer. One approach is to use multiple mesh resonators, which are discussed in the set of papers by Pradhan and co-workers (Saksena *et al.*, 1969; Pradhan, 1971; Pradhan and Garg, 1976, 1977; Garg and Pradhan, 1978). The advantage of using meshes instead of polarizers is that meshes have polarization-independent response at normal incidence. As we discussed in Section IX, it is desirable to use circular polarization to code the incident and reflected power. Furthermore, meshes allow the Fabry–Pérot resonator to have a reflection minimum on-resonance. Thus, meshes are the optical elements of choice to build a reflection mode spectrometer with polarization coding. An interesting alternative implementation of polarization-coding techniques is afforded by induction mode spectroscopy. Here, the sample is excited in one linear polarization state and the ESR sample causes a response in the orthogonal polarization state. The signal in the orthogonal arm may be easily separated from the incident radiation by means of a grid polarizer. Portis and Teaney (1958) and Teaney, Portis, and Klein (1961) have implemented an induction mode bridge with a cylindrically symmetric TE_{111} cavity at X-band. The quasi-optical analog is a cylindrically symmetric Fabry–Pérot resonator with a symmetrical, flat mesh for coupling. A quasioptical induction mode spectrometer is discussed briefly by Smith *et al.* (1995). See also Earle *et al.* 1996c).

Treatments of wire meshes can be found in the books of Chantry (1984) and in Goldsmith (1982, Chap. 5) and Holah (1982). These treatments are based mainly on the original work of Ulrich and co-workers (Ulrich *et al.*, 1963; Ulrich, 1968, 1979), who derived an equivalent circuit analysis for wire meshes that works quite well in practice.

The power transmissivity of a wire mesh τ_i is given by

$$\tau_i = \frac{R_z^2 + \Omega^2 Z_0^2}{\left(1 + R_z^2\right) + \Omega^2 Z_0^2} \tag{101}$$

where Z_0 is a characteristic impedance determined by the mesh thickness and spacing,

$$Z_0 = \left[\ln \csc\left(\frac{\pi a}{2g}\right)\right]^{-1} \tag{102}$$

R_z is a dimensionless correction for ohmic resistance in the mesh material and Ω is the "generalized frequency"

$$\Omega = \frac{\omega \omega_0}{\omega^2 - \omega_0^2} \tag{103}$$

The quantity R_z should not be confused with the reflectivity of the surface, which is given by $R_i = 1 - \tau_i$, where τ_i is defined by eqs. (101)–(105). The wire mesh geometry is shown in Fig. 9a. In Eq. (103), $\omega = g/\lambda$ and ω_0 is a dimensionless correction factor near unity, which has been empirically found to be (Ulrich *et al.*, 1963; Ulrich, 1968, 1979)

$$\omega_0 = 1 - 0.27\left(\frac{a}{g}\right) \tag{104}$$

The correction for ohmic resistance can be estimated from the bulk resistivity ρ of the metal as

$$R_z = \left(\frac{4\pi\epsilon c \rho}{\lambda}\right)\frac{\eta}{2} \tag{105}$$

where η is a geometric factor equal to $g/2a$ for inductive mesh and ϵ is the substrate permittivity. The correction is negligible for metals of practical importance in the near-millimeter band. Figure 8b plots the reflectivity as a function of mesh spacing and wire width for Ni mesh at 250 GHz (λ = 1.2 mm).

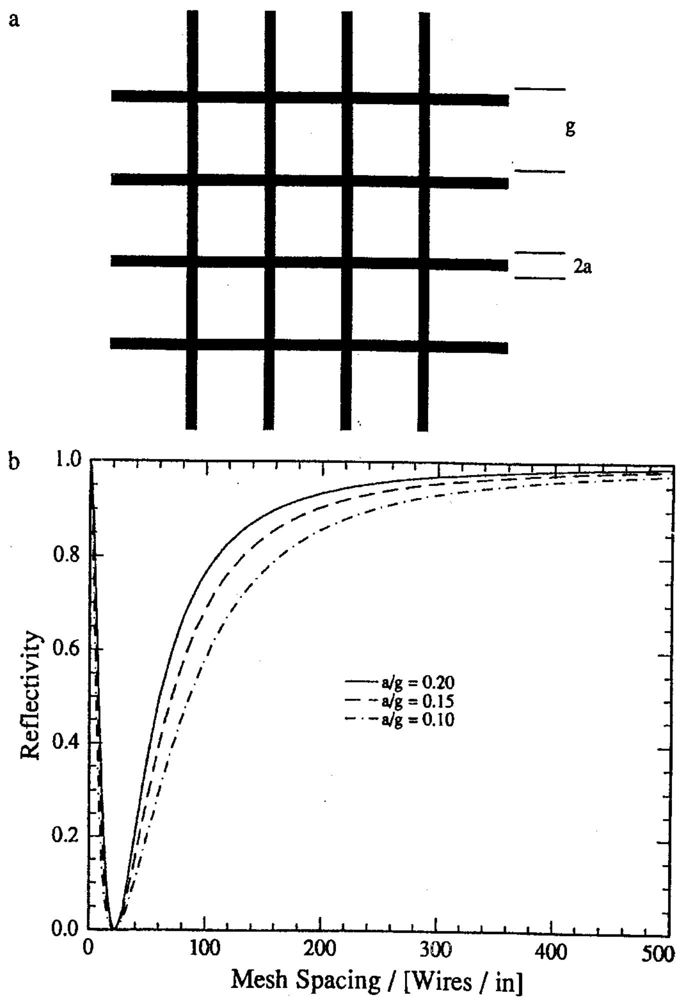

FIG. 9. (a) Geometry of mesh reflectors. (b) Reflectivity versus mesh spacing and wire width.

We will now investigate a method for adjusting the coupling of the resonator to the input optical waveguide. The reflectivities of the mirrors that define the resonator determine the degree of coupling to the incident

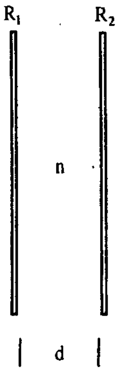

FIG. 10. Planar Fabry–Pérot interferometer with mirrors of different reflectivity R_1 and R_2. The approximate condition for resonance is $nkd = q\pi$, where q is an integer.

radiation, as we will show. The optical layout of a planar Fabry–Pérot interferometer is shown in Fig. 10, where we assume that a dielectric of thickness d and index of refraction n has identical reflective coatings, which give rise to surface reflectivities R_1 and R_2 assumed equal.

The classical response of such a Fabry–Pérot interferometer is shown in Fig. 11. Transmission maxima correspond to reflection minima and vice versa. If the reflectivities of the two mirrors are unequal, then the reflected power has a minimum that is different from zero. This case is illustrated by Fig. 12a, where one mirror has a variable reflectivity $0.7 < R_1 < 0.9$ and the other mirror has a fixed reflectivity $R_2 = 0.8$.

We will now derive explicit mathematical expressions from which the curves in Figs. 11 and 12 are derived. We consider first a two mirror system where the amplitudes of reflection and transmission are given by r_i and t_i, respectively, where the subscript i indicates mirror 1 or mirror 2. For mirrors of high reflectivity, there will be many reflections within the interferometer that will cause the apparent beam radius to grow. This effect is shown in Fig. 12b, which demonstrates how the beam radius grows with each round trip in the interferometer. We will account for this effect quantitatively in the sequel.

At each mirror, the reflected or transmitted wave is multiplied by a factor of r_i or t_i respectively. If the resonator has a large finesse, there will be many reflections and transmissions. A simple case where $r_1 = r_2 = r$ and $t_1 = t_2 = t$ is shown in Fig. 12b. Each reflected wave picks up an amplitude coefficient r and each transmitted wave picks up a coefficient t. The individual waves are called partial waves. It is the sum of all of the partial waves shown in Fig. 12b that gives the resonator its characteristic

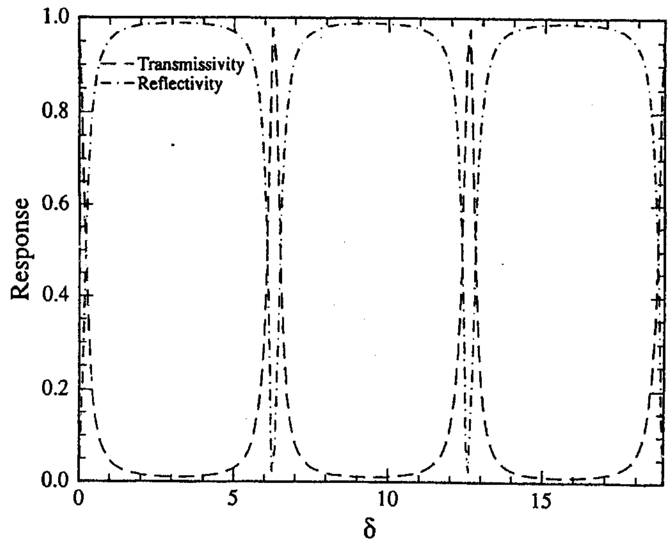

FIG. 11. Reflectivity and transmissivity of a planar Fabry–Pérot $R = 0.8$. The transmissivity is indicated by the dash-dot line; the reflectivity is indicated by the dashed line.

response. Before we can perform the partial wave sum we must include a phase factor $e^{i\delta}$ to allow for a relative phase shift between partial waves that have made a round trip in the resonator. Returning to the case where the reflectivities of the two mirrors differ, we have, for the transmission response,

$$\begin{aligned} E_t &= t_1 t_2 \left[1 + r_1 r_2 e^{i\delta} + r_1^2 r_2^2 e^{2i\delta} + \cdots \right] E_i \\ &= \frac{t_1 t_2}{1 - r_1 r_2 e^{i\delta}} E_i \end{aligned} \tag{106}$$

$$\begin{aligned} \tau_{12} &= \frac{E_t}{E_i} \\ &= \frac{t_1 t_2}{1 - r_1 r_2 e^{i\delta}} \end{aligned} \tag{107}$$

where we used the identity $\sum_{p=0}^{\infty} z^p = 1/(1 - z)$ when $|z| < 1$.

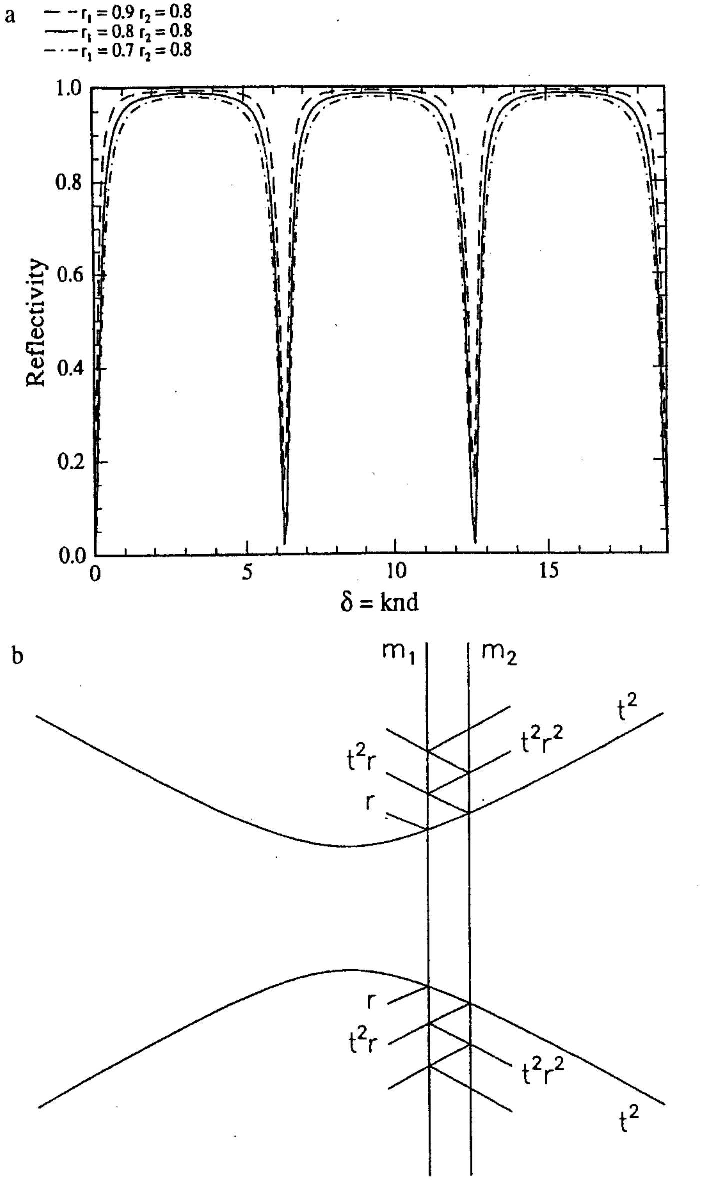

FIG. 12. Fabry–Pérot resonator with one mirror of variable reflectivity r_1 and one mirror of variable reflectivity r_2. (a) Dashed line $r_1 = 0.9$; solid line $r_1 = 0.8$; dot-dash line $r_1 = 0.7$ and $r_2 = 0.8$. (b) Planar Fabry–Pérot interferometer that shows the effect of beam growth between the mirrors. The transmitted beam is a superposition of all the partial waves to the right of m_2.

The amplitude of reflection may be found by following a similar procedure. Up to an unimportant phase factor, we may write

$$E_r = \{r_1 - r_2 t_1^2 e^{i\delta}[1 + r_1 r_2 e^{i\delta} + r_1^2 r_2^2 e^{2i\delta} + \cdots]\}E_i$$

$$= \frac{r_1 - r_2 e^{i\delta}}{1 - r_1 r_2 e^{i\delta}} E_i \tag{108}$$

$$\rho_{12} = \frac{E_t}{E_i}$$

$$= \frac{r_1 - r_2 e^{i\delta}}{1 - r_1 r_2 e^{i\delta}} \tag{109}$$

The reflectivity and transmissivity of the resonator may be found by calculating the squared modulus of the amplitude of reflection and transmission. We find

$$\mathscr{R} = |\rho_{12}|^2$$

$$= \frac{R_1 + R_2 - 2\sqrt{R_1 R_2}\cos\delta}{1 + R_1 R_2 - 2\sqrt{R_1 R_2}\cos\delta} \tag{110}$$

$$\mathscr{T} = |\tau_{12}|^2$$

$$= \frac{T_1 T_2}{1 + R_1 R_2 - 2\sqrt{R_1 R_2}\cos\delta} \tag{111}$$

If we set $R_1 = R_2 = R$, we recover the standard result for identical mirrors (Born and Wolf, 1980, p. 325).

We define an effective mirror reflectivity for the two mirror resonator as $R_{\mathrm{eff}} = \sqrt{R_1 R_2}$. Using this definition and the well-known half-angle identity $\sin^2(\delta/2) = (1 - \cos\delta)/2$, we rewrite the resonance denominator in the standard form, namely, $(1 - R_{\mathrm{eff}})^2 + 4R_{\mathrm{eff}}\sin^2(\delta/2)$. If, in addition, we define the coefficient of finesse $F_{\mathrm{eff}} = 4R_{\mathrm{eff}}/(1 - R_{\mathrm{eff}})^2$, the transmissivity becomes

$$\mathscr{T} = \frac{T_1 T_2/(1 - R_{\mathrm{eff}})^2}{1 + F_{\mathrm{eff}}\sin^2(\delta/2)} \tag{112}$$

$$\approx \frac{1}{1 + F_{\mathrm{eff}}\sin^2(\delta/2)} \tag{113}$$

if $R_1 \approx R_2$. In this case, the transmission maxima are spaced by 2π in δ and the half-power points occur at $\delta = 2m\pi \pm (\delta_{1/2}/2)$. If the coefficient of finesse is sufficiently large, the ratio of the fringe separation to the width is

$$\begin{aligned}\mathcal{F}_{\text{eff}} &= \frac{2\pi}{\delta_{1/2}} \\ &\approx \frac{\pi\sqrt{F_{\text{eff}}}}{2} \qquad (114)\end{aligned}$$

where $\mathcal{F}_{\text{eff}}$ is the effective resonator finesse. If we could vary R_1, say, then the finesse of the resonator would be adjustable.

Suppose that the first mirror is actually constructed from two mirrors with variable phase factor δ_1. The reflectivity and transmissivity of such a mirror are given by the foregoing formulae; the overall reflectivity and transmissivity of the composite mirror/single mirror will be written by substituting the expressions for the amplitude of reflection and transmission for the composite mirror into the expressions for the amplitudes of transmission and reflection of the equivalent two mirror system, described by a phase factor δ_2. This is essentially an iterative calculation, and the results (Garg and Pradhan, 1978) are

$$\begin{aligned}\mathcal{T}_3 = (T_1T_2T_3)/\big[&1 + R_1R_2 + R_2R_3 + R_3R_1 - 2\sqrt{R_1R_2}(1 + R_3)\cos\delta_1 \\ &-2\sqrt{R_2R_3}(1 + R_1)\cos\delta_2 + 2R_2\sqrt{R_3R_1}\cos(\delta_1 - \delta_2) \\ &+2\sqrt{R_3R_1}\cos(\delta_1 + \delta_2)\big] \qquad (115)\end{aligned}$$

$$\begin{aligned}\mathcal{R}_3 = [\mathcal{T}_3/(T_1T_2T_3)]\big[&R_1 + R_2 + R_3 + R_1R_2R_3 - 2\sqrt{R_1R_2}(1 + R_3)\cos\delta_1 \\ &-2\sqrt{R_2R_3}(1 + R_1)\cos\delta_2 + 2R_2\sqrt{R_3R_1}\cos(\delta_1 - \delta_2) \\ &+2\sqrt{R_3R_1}\cos(\delta_1 + \delta_2)\big] \qquad (116)\end{aligned}$$

where

$$\delta_1 = \frac{4\pi}{\lambda}s_1 - (\phi_1 + \phi_2)$$

$$\delta_2 = \frac{4\pi}{\lambda}s_2 - (\phi_1 + \phi_2)$$

s_1 = the separation between mirrors 1 and 2

s_2 = the separation between mirrors 2 and 3

and ϕ_1 and ϕ_2 are additional phase shifts suffered (or enjoyed) by the partial waves upon reflection from the grids. The additional phase shifts may be calculated for a particular mesh from the expressions of Saksena et al. (1969). For normal incidence, small grid spacing-to-wavelength ratio, and mirror separations on the order of half a wavelength or larger, the correction terms ϕ_1 and ϕ_2 are on the order of 1% or less (Saksena et al., 1969).

XI. Optimization of Resonators

Using the tools developed in Section X, we will now address considerations for choosing the optimum dimensions and parameters of a coupled Fabry–Pérot interferometer (CFPI) shown in Fig. 13.

The design beam waist in the cavity and the design reflectivity of the CFPI meshes are very closely related. The choice of these parameters for optimal spectrometer sensitivity is largely governed by two competing effects. First, Eq. (73) tells us that the minimum detectable number of spins N_{min} is inversely proportional to the loaded Q. The loaded Q in turn is proportional to the cavity finesse, which increases with mesh reflectivity. Therefore, meshes of higher reflectivity lead to smaller N_{min}. On the other hand, higher mesh reflectivities require larger beam waists as shown in Eq. (118). A larger beam waist will result in a smaller B_1 field for the millimeter waves at the sample [cf. Eq. (80)]. Using Eqs. (73) and (80), we see that a smaller B_1 will reduce the sensitivity for nonsaturated lines. Clearly, a careful consideration of the balance between these opposing effects is required to arrive at sensible design parameters.

A given mesh reflectivity imposes a lower bound for the beam-waist radius, below which appreciable coupling losses can occur. The basic problem is that a Gaussian beam will continue to diverge upon repeated reflection within a planar interferometer as shown in Fig. 12b. If the spherical mirror of the cavity is designed to match the original (input) beam waist, beam divergence will cause a mismatch at the output, which

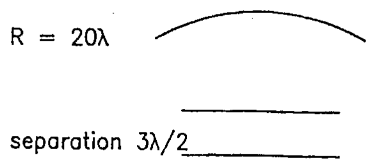

FIG. 13. Schematic of a variable-coupling semiconfocal Fabry–Pérot sample cavity. Varying the separation of the two wire meshes changes the apparent reflectivity. The curved mirror refocuses the radiation.

essentially appears as radiative losses of the cavity. Arnaud *et al.* (1974) studied this effect extensively. For mirrors of reflectivity R_M and spacing d, the coupling efficiency of an input beam with wavelength λ and confocal length z_0 to an output beam with the same parameters is given by $N_0 = |C_0|^2$, where

$$C_0 = (1 - R_M)^2 \sum_{m=0}^{\infty} \frac{R_M^{2m} \exp(im4\pi d/\lambda)}{1 - imd/z_0} \tag{117}$$

Arnaud *et al.* gave an expression that leads to the following criterion for restricting the coupling loss to 1 dB or less:

$$w_0 \geq 0.2\sqrt{\frac{4\pi d\lambda}{(1 - R_M)}} \tag{118}$$

Optimization of R_M must take into account the sample cavity finesse, which may be expressed in terms of R_M and R_S, where R_S is the reflectivity of the spherical mirror shown in Fig. 13, using Eq. (110) with $R_{\text{eff}} = \sqrt{R_{\text{CFPI}} R_S}$, and R_{CFPI} is taken to be the maximal reflectivity of the coupling FPI for a given R_M:

$$R_{\text{CFPI}} = \frac{4R_M}{(1 + R_M)^2} \tag{119}$$

Equation (80) tells us that $\bar{B}_1 \propto \sqrt{\mathcal{F}}/w_0$ at the sample, and we can take the simple initial approach of optimizing the ratio $\sqrt{\mathcal{F}(R_M)}/w_0(R_M)$, as calculated from Eqs. (119), (118), and (110). Figure 14 shows this ratio plotted versus R_M for a range of spherical mirror reflectivities R_S. We also show the $\sqrt{\mathcal{F}}/w_0$ ratio for the current transmission mode resonator. From Fig. 14 we can see that an optimum R_M value does exist, which depends on the reflectivity of the spherical mirror. For a transmission mode resonator, a conservative design with modest R_S values near 0.90 would place R_M in the range of 0.78–0.82. In a reflection mode design, in which $R_S \approx 1$, significantly higher mesh reflectivities may be possible, which also will require larger beam waists. In that case, it will be necessary to take extra precautions to ensure that the sample is sufficiently large so that the filling factor is not reduced. In Section VIII, we discussed the reasons for using nonoptimum B_1 and $\mathcal{F}$ in the current transmission mode spectrometer. In the future, however, we plan to exploit the higher B_1s that will be available from the quasioptical coupling design.

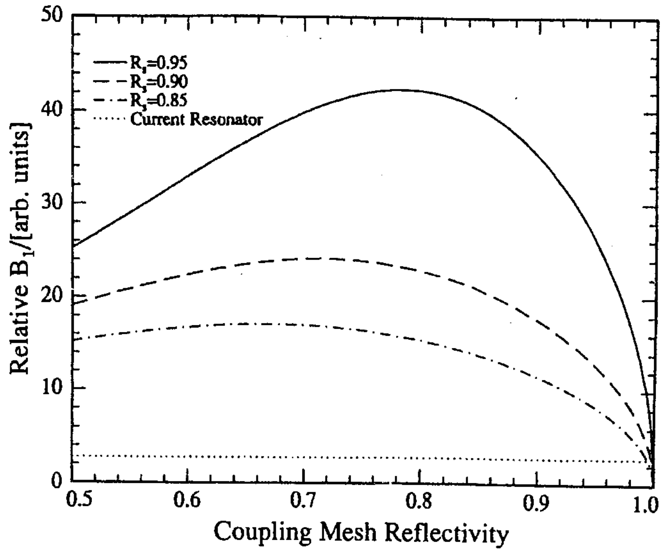

FIG. 14. Relative B_1 intensity in the coupling Fabry–Pérot interferometer (CFPI) as a function of R_M. For a given R_S, the proper choice of mesh reflectivity of the flat mirror can enhance B_1 at the sample significantly.

XII. Summary

We have presented a complete analysis of the Cornell mm-wave spectrometer using quasioptical techniques. We also have developed a quasioptical formalism with sufficient flexibility to predict the performance of a novel reflection mode spectrometer with variable input coupling and transmit–receive duplexing based on polarization coding and we present a practical realization of these design concepts in Earle *et al.* (1996b). At every stage we have chosen parameters that correspond to practical performance values and measured response.

The treatment given here is self-contained, but the references contain many useful extensions of our results and alternative treatments that may deepen the reader's understanding. We have tried, where possible, to take advantage of EPR spectroscopists' knowledge of microwave circuits and analysis. As high-field ESR becomes more common, we predict that analogies from other fields will continue to be a useful method for extending the generality and utility of the method. Implementing the advanced techniques discussed in Sections IX–XI will give significant improvements in signal-to-noise ratio as we have demonstrated elsewhere (Earle *et al.*, 1996b).

Appendix: Higher Order Gaussian Beam Modes

In this Appendix, we will develop the mathematical background necessary to study higher order Gaussian beam modes. We also will outline how certain integrals that arise in beam mode analysis may be evaluated. Because this material is a compilation from several sources, the original works should be consulted for further details.

The vector Helmholtz equation may be rewritten in a form suitable for evaluation in curvilinear coordinates as follows, using well-known vector identities:

$$\nabla(\nabla \cdot \mathbf{F}) - \nabla \times \nabla \times \mathbf{F} + k^2\mathbf{F} = 0 \qquad (120)$$

where **F** is a vector function of position. Equation (120) is a set of coupled equations in a general curvilinear coordinate system. In cylindrical coordinates, the $\hat{\rho}$ and $\hat{\varphi}$ components decouple from the $\hat{z}$ component when **F** is written in the form

$$\mathbf{F} = \left[\hat{\rho}\begin{Bmatrix}\cos m\varphi \\ \sin m\varphi\end{Bmatrix} + \hat{\varphi}\begin{Bmatrix}-\sin m\varphi \\ \cos m\varphi\end{Bmatrix}\right] f_{m-1}(\rho, z) \qquad (121)$$

where m is a positive integer. We call such a function a *transverse* vector function. The Hertz potentials for the dipole or fundamental Gaussian beam discussed in Section III are a special case of transverse vector function with $m = 1$. In that case, f_0 is the fundamental Gaussian beam mode. Superpositions of transverse vector functions that satisfy the vector Helmholtz equation are also solutions of the vector Helmholtz equation because it is a linear vector equation. We can construct circularly polarized transverse electromagnetic fields in this way, for example.

It is possible to show that the vector Helmholtz equation for a transverse vector function reduces to the following equation for the scalar function $f_{m-1}(\rho, z)$ in cylindrical coordinates:

$$\left(\frac{\partial^2}{\partial\rho^2} + \frac{1}{\rho}\frac{\partial}{\partial\rho} - \frac{(m-1)^2}{\rho^2} + \frac{\partial^2}{\partial z^2} + k^2\right) f_{m-1}(\rho, z) = 0 \quad (122)$$

We now see that our choice of index on f_{m-1} is more than a convenient label: it characterizes the radial and longitudinal dependence of the scalar part of *transverse* solutions of the vector Helmholtz equation.

The scalar Helmholtz equation in cylindrical coordinates has the form

$$\left(\frac{\partial^2}{\partial\rho^2} + \frac{1}{\rho}\frac{\partial}{\partial\rho} + \frac{1}{\rho^2}\frac{\partial^2}{\partial\varphi^2} + \frac{\partial^2}{\partial z^2} + k^2\right) g(\rho, \varphi, z) = 0 \quad (123)$$

We may rewrite Eq. (123) so that it is identical with Eq. (122) by the following choice for the scalar function $g(\rho, \varphi, z)$:

$$g(\rho, \varphi, z) = f_{lp}(\rho, z)e^{il\varphi} \qquad (124)$$

where we have set $l = m - 1$ and p is an additional mode number that characterizes higher order radial modes, as we will show in the sequel.

We may now derive the electromagnetic field of higher order transverse Gaussian beam modes. In order to do so, we will use a technique developed for Cartesian coordinates described in Marcuse (1975), but adapted to cylindrical symmetry. For a system with cylindrical symmetry, we may take a trial solution of the form

$$g = f_{lp}\left(\frac{\rho}{w(z)}\right)\exp\left(i\left(P(z) + \frac{k\rho^2}{2q(z)} + l\varphi + \Phi(z)\right)\right) \qquad (125)$$

where Φ is an additional phase correction to the fundamental that will be shown to depend upon the radial and azimuthal mode numbers p and l, respectively, where φ is the azimuthal angle. The function g corresponds to the scalar function ψ in Section III. This is a more general trial function than the one we chose for the fundamental Gaussian beam mode in Section III. The dipole field discussed in Section III is a special case of Eq. (125), where $l = 0$, $\Phi(z) = 0$, and $f_{lp} = 1$.

Upon writing the scalar Helmholtz equation in cylindrical coordinates and dropping the $\partial^2 g/\partial z^2$ term as discussed in Section III, we find the following equation for f_{lp}:

$$f''_{lp}(\xi) - 2\xi f'_{lp}(\xi) + \frac{1}{\xi}f'_{lp} - \frac{l^2}{\xi^2} - kw^2(z)\dot{\Phi}f_{lp} = 0 \qquad (126)$$

where $\xi = \sqrt{2}(\rho/w(z))$ primes indicate differentiation with respect to ξ, the overdot indicates differentiation with respect to z, and Eq. (15) has been used to simplify Eq. (126). Note that the use of Eq. (126) implies that the quantities derived from it, that is, $R(z)$, the radius of curvature of the Gaussian beam, and $w(z)$ the beam radius, are the same for the fundamental and all higher modes of the Gaussian beam.

In order to find an explicit form for f_{lp}, we may use the trial function $f_{lp} = \xi^l L_p^l(\xi^2)$. After a tedious but straightforward calculation, we find

$$4x \frac{d^2 L_p^l}{dx^2} + 4(l + 1 - x)\frac{dL_p^l}{dx} - 2lL_p^l - kw^2(z)\dot{\Phi} L_p^l = 0 \quad (127)$$

where $x = \xi^2$. If we make the substitution $4p + 2l + kw^2(z)\dot{\Phi} = 0$, then Eq. (127) becomes Laguerre's differential equation

$$x \frac{d^2 L_p^l}{dx^2} + (l + 1 - x)\frac{dL_p^l}{dx} + pL_p^l = 0 \quad (128)$$

Solving for Φ, we obtain

$$\Phi = -(2p + l)\tan^{-1}\left(\frac{z}{z_0}\right) \quad (129)$$

Putting all the pieces together, we obtain for the cylindrical Gaussian beam modes

$$u = \frac{w_0}{w(z)}\left(\sqrt{2}\,\frac{\rho}{w(z)}\right)^l L_p^l\left(2\frac{\rho^2}{w^2(z)}\right)\exp\left(-\left(\frac{\rho}{w(z)}\right)^2\right)$$
$$\times \exp\left(i\left[kz + l\varphi - (2p + l + 1)\tan^{-1}\left(\frac{z}{z_0}\right) + \frac{k\rho^2}{2R(z)}\right]\right) \quad (130)$$

We have now successfully reduced the vector Helmholtz equation to the scalar Helmholtz equation for transverse fields. Under the conditions derived in Section III, transverse fields are often an accurate description of a Gaussian beam. In order to study the effects of diffraction on transverse fields, we note that scalar diffraction theory is based on the scalar Helmholtz theory (Born and Wolf, 1980, pp. 370–386). Thus, we may use scalar diffraction theory with the function u to elucidate the effects of diffraction on Gaussian beams that are well approximated by transverse fields.

At this point, it will be useful to recall some of the properties of the Laguerre polynomials. The Laguerre polynomials are a set of orthogonal polynomials that satisfy the differential equation (Gradshteyn and Ryzhik, 1980, pp. 1037–1039)

$$x\frac{d^2u}{dx^2} + (\alpha - x + 1)\frac{du}{dx} + nu = 0 \quad (131)$$

A general form for the Laguerre polynomials is given by

$$L_n^\alpha = \frac{1}{n!}e^x x^{-\alpha}\frac{d^n}{dx^n}(e^{-x}x^{n+\alpha}) \quad (132)$$

$$= \sum_{m=0}^{n}(-1)^m\binom{n+\alpha}{n-m}\frac{x^m}{m!} \quad (133)$$

where $\binom{n+\alpha}{n-m}$ is a binomial coefficient, n is the radial mode number, and α is the azimuthal mode number. Explicit expressions for the lowest order modes are

$$L_0^\alpha(x) = 1 \quad (134)$$
$$L_1^\alpha(x) = \alpha + 1 - x \quad (135)$$
$$L_2^\alpha(x) = \tfrac{1}{2}(1 - \alpha)(2 + \alpha) - (2 + \alpha)x - \tfrac{1}{2}x^2 \quad (136)$$

We will be interested in the properties of so-called Laguerre functions (van Nie, 1964) as well. They have the functional form

$$R_n^\alpha(x^2) = x^\alpha \exp(-\tfrac{1}{2}x^2)L_n^\alpha(x^2) \quad (137)$$

and are orthogonal in the sense that

$$\int_0^\infty R_n^\alpha(x^2)R_m^\alpha(x^2)\,d(x^2)$$
$$= \int_0^\infty x^{2\alpha}\exp(-x^2)L_n^\alpha(x^2)L_m^\alpha(x^2)\,d(x^2) \quad (138)$$
$$= \delta_m^n\frac{(m+n)!}{n!} \quad (139)$$

where the final equality follows from Gradshteyn and Ryzhik (1980, pp. 843–848) and δ_m^n is the Kronecker symbol. The previous integral is also useful for calculating the mode purity of a beam launched from a scalar feed (Wylde, 1984).

The following integral from Gradshteyn and Ryzhik (1980, pp. 843–848) is useful in the evaluation of the Fourier transform of a Laguerre function as well as its convolution with a complex-valued Gaussian (Martin and Bowen, 1993):

$$\int_0^\infty x^{\nu+1}\exp(-\beta x^2)L_n^\nu(\alpha x^2)J_\nu(xy)\,dx$$
$$= 2^{-\nu-1}\beta^{-\nu-n-1}(\beta - \alpha)^n y^\nu \exp\left(-\frac{y^2}{4\beta}\right)L_n^\nu\left[\frac{\alpha y^2}{4\beta(\alpha - \beta)}\right] \quad (140)$$

Interferometer design often requires evaluation of the coupling between Gaussian beams within the interferometer (LeSurf, 1987). Because the integrand can always be reduced to a polynomial times a Gaussian in such calculations presents no analytical challenges. However, we can simplify even further; the orthogonality of the Laguerre functions upon integration over the azimuth ensures that the polynomial is in powers of x^2. The following well-known integral is useful in such calculations on the assumption that truncation effects may be neglected:

$$\int_0^\infty t^{2n+1}\exp(-at^2)\,dt = \frac{n!}{2a^{n+1}} \qquad (141)$$

If truncation effects may not be neglected, the integral may be written as $\int_0^1 x^p e^{-x}\,dx$, which may be evaluated by integration by parts.

The results collected here allow evaluation of the effect of higher order modes in the design of quasioptical systems. It is important to note, however, that the optimum performance conditions usually obtain when the only significant mode is the fundamental L_0^0 mode.

ACKNOWLEDGMENTS

This work was supported by NIH grant RR07126 and NSF grant CHE9313167. KAE thanks P. F. Goldsmith, R. Compton, M. Wengler, and G. M. Smith for many useful discussions.

REFERENCES

Abragam, A., and Bleaney, B. (1970). "Electron Paramagnetic Resonance of Transition Ions." Oxford Univ. Press, London.
Anan'ev, Yu. A. (1992). "Laser Resonators and the Beam Divergence Problem," pp. 10–72. Hilger, Bristol.
Arnaud, J. A., Saleh, A. M., and Ruscio, J. T. (1974). *IEEE Trans. Microwave Theory Tech.* **MTT-22**, 468–493.
Barnes, J. P., and Freed, J. H. (1996). Unpublished manuscript.
Barra, A. L., Brunel, L.-C., and Robert, J. B. (1990). *Chem. Phys. Lett.* **165**, 107.
Blaney, T. G. (1980). *In* "Infrared and Millimeter Waves: Submillimeter Techniques" (K. J. Button, ed.), Vol. 3, Chap. 1. Academic Press, New York.
Born, M., and Wolf, E. (1980). "Principles of Optics," 6th ed. Pergamon, Elmsford, NY.
Boucher, D., Bocquet, R., Chen, W., and Burie, J. (1993). *Int. J. Infrared Millimeter Waves* 14, 1889–1903.
Bouwkamp, C. J., and Casimir, H. B. G. (1954). *Physica* **20**, 539–554.
Bresgunov, A. Yu., Dubinskii, A. A., Krimov, V. N., Petrov, Yu. G., Poluektov, O. G., and Lebedev, Ya. S. (1991). *Appl. Magn. Reson.* **2**, 715.
Budil, D. E., Earle, K. A., Lynch, W. B., and Freed, J. H. (1989). *In* "Advanced EPR: Applications in Biology and Biochemistry" (A. J. Hoff, ed.), Chap. 8. Elsevier, New York.
Burghaus, O., Toth-Kischkat, A., Klette, R., and Möbius, K. (1988). *J. Magn. Reson.* **80**, 383–385.

Campbell, J. P., and DeShazer, L. (1969). *J. Opt. Soc. Amer.* **59**, 1427–1429.
Chantry, G. W. (1984). "Long-wave Optics," Vols. 1 and 2. Academic Press, New York.
Chedester, R. (1988). Private communication.
Chu, T. S., and Turrin, R. H. (1973). *IEEE Trans.* **AP-21**, 339–345.
Debye, P. (1909). *Ann. Phys.* **30**, 57–136.
Degenford, J. E., and Coleman, P. D. (1966). *Proc. IEEE* **54**, 520–522.
Deschamps, G. A. (1971). *Electron. Lett.* **7**, 684–685.
Earle, K. A. (1991). Unpublished notes.
Earle, K. A. (1994). Ph.D. thesis, Cornell University.
Earle, K. A., Budil, D. E., and Freed, J. H. (1993). *J. Phys. Chem.* **97**, 13289–13297.
Earle, K. A., and Freed, J. H. (1995). *Proceedings of the SPIE. Millimeter and Submillimeter Waves II* **2558**, 86–97.
Earle, K. A., Moscicki, J. K., Ge, M., Budil, D. E., and Freed, J. H. (1994). *Biophys. J.* **66**, 1213–1221.
Earle, K. A., Polimeno, A., Moscicki, J. K., and Freed, J. H. (1996a). Unpublished manuscript.
Earle, K. A., Tipikin, D. S., and Freed, J. H. (1996b). *Rev. Sci. Inst.* **67**, 2502–2513.
Earle, K. A., Tipikin, D. S., and Freed, J. H. (1996c) *In* Proceedings of the 38th Rocky Mountain Conference on Analytical Chemistry.
Erickson, N. R. (1987). *Int. J. Infrared Millimeter Waves* **8**, 1015–1025.
Garg, R. K., and Pradhan, M. M. (1978). *Infrared Phys.* **18**, 292–298.
Goldsmith, P. F. (1982). *In* "Infrared and Millimeter Waves: Systems and Components" (K. J. Button, ed.), Vol. 6, Chap. 5. Academic Press, New York.
Goldsmith, P. F. (1992). *IEEE Proc.* **80**, 1729–1747.
Goy, P. (1983). *In* "Infrared and Millimeter Waves: Electromagnetic Waves in Matter, Part I" (K. J. Button, ed.), Vol. 8, Chap. 8. Academic Press, New York.
Gradshteyn, I. S., and Ryzhik, I. M. (1980). "Table of Integrals Series and Products," 6th ed. Academic Press, New York.
Griffin, R. G. (1995). Private communication.
Grinberg, O. Ya., Dubinskii, A. A., and Lebedev, Ya. S. (1983). *Russian Chem. Rev.* **52**, 850.
Haindl, E., Möbius, K., and Oloff, H. (1985). *Z. Naturforsch.* **40a**, 169.
Hecht, E., and Zajac, A. (1979). "Optics." Addison-Wesley, Reading, MA.
Holah, G. D. (1982). *In* "Infrared and Millimeter Waves: Systems and Components" (K. J. Button, ed.), Vol. 6, Chap. 6. Academic Press, New York.
Howard, J., Peebles, W. A., and Luhmann, N. C., Jr. (1986). *Int. J. Infrared Millimeter Waves* **7**, 1591–1603.
Jackson, J. D. (1975). "Classical Electrodynamics," 2nd ed., pp. 128–131. Wiley, New York.
Kogelnik, H. (1965). *Bell Syst. Tech. J.* **44**, 455–494.
Kogelnik, H., and Li, T. (1966). *Appl. Opt.* **5**, 1550–1567.
Kraus, J. D. (1950). "Antennas," pp. 382–890. McGraw-Hill, New York.
Lebedev, Ya. (1990). *In* "Modern Pulsed and Continuous-Wave Electron Spin Resonance" (L. Kevan and M. Bowman, eds.), Chap. 8. Wiley, New York.
LeSurf, J. C. G. (1987). *Infrared Phys.* **28**, 129–137.
LeSurf, J. C. G. (1990). "Millimeter-Wave Optics, Devices, and Systems." Hilger, Bristol.
LeSurf, J. C. G. (1993). "Gaussian Beam Mode Optics for Millimeter-Wave and Terahertz Systems." Int. Soc. Opt. Eng., Bellingham, WA.
Love, A. W. (1976). "Electromagnetic Horn Antennas." IEEE Press, New York.
Lynch, W. B., Boorse, R. S., and Freed, J. H. (1993). *Amer. Chem. Soc.* **115**, 10909–10915.
Lynch, W. B., Earle, K. A., and Freed, J. H. (1988). *Rev. Sci. Instrum.* **59**, 1345–1351.
Marcuse, D. (1975). "Light Transmission Optics." Van Nostrand-Reinhold, New York. See particularly Chaps. 5 and 6.

Martin, D. H., and Bowen, J. W. (1993). *IEEE Trans. Microwave Theory Tech.* **MTT-41**, 1676–1690.

Martin, D. H., and LeSurf, J. C. G. (1978). *Infrared Phys.* **18**, 405–412.

Milligan, T. (1985). "Modern Antenna Design," pp. 190–206. McGraw-Hill, New York.

Moll, H. P. (1994). "Electron Paramagnetic Resonance in High Magnetic Field using Far Infrared Lasers: Electron Spin Echoes at 604 GHz." Diplomarbeit, Universität Konstanz.

Montgomery, C. G., Dicke, R. H., and Purcell, E. M. (1948). "Principles of Microwave Circuits," pp. 238–239. McGraw-Hill, New York.

Moore, E. (1988). Private communication.

Murphy, J. A. (1987). *Int. J. Infrared Millimeter Waves* **8**, 1165–1187.

Padman, R. (1979). *IEEE Trans. Antennas Propagat.* **AP-26**, 741.

Poole, C., Jr. (1967). "Electron Spin Resonance: A Comprehensive Treatise on Experimental Techniques." p. 550. Wiley–Interscience, New York.

Portis, A. M., and Teaney, D. T. (1958). *J. Appl. Phys.* **29**, 1692–1698.

Pradhan, M. M. (1971). *Infrared Phys.* **11**, 241–245.

Pradhan, M. M., and Garg, R. K. (1976). *Infrared Phys.* **16**, 449–452.

Pradhan, M. M., and Garg, R. K. (1977). *Infrared Phys.* 17, 253–256.

Prisner, T. F., Un, S., and Griffin, R. G. (1992). *Israel J. Chem.* **32**, 357–363.

Risser, J. R. (1949). "Microwave Antenna Theory and Design," Chap. 11. McGraw-Hill, New York.

Saksena, B. D., Pahwa, D. R., Pradhan, M. M., and Lal, K. (1969). *Infrared Phys.* **9**, 43–52.

Schell, R. G., and Tyras, G. (1971). *J. Opt. Soc. Amer.* **61**, 31–35.

Schneider, M. V. (1982). *In* "Infrared and Millimeter Waves: Systems and Components" (K. J. Button, ed.), Vol. 6, Chap. 4. Academic Press, New York.

Slepian, D. (1964). *Bell Syst. Tech. J.* **43**, 3009–3057.

Smith, G. M., LeSurf, J. C. G., Mitchell, R. H., and Reidy, P. C. (1995). *In* Proceedings of the MTT-S. IEEE Press, New York.

Teaney, D. T., Klein, M. P., and Portis, A. M. (1961). *Rev. Sci. Inst.* **32**, 721–729.

Thomas, B. M. (1978). *IEEE Trans. Antennas Propagat.* **AP-26**, 367–377.

Tipikin, D. S., Earle, K. A., and Freed, J. H. (1996). Unpublished manuscript.

Tudisco, O. (1988). *Int. J. Infrared Millimeter Waves* **9**, 41–53.

Ulrich, R. (1968). *Appl. Opt.* **7**, 1981.

Ulrich, R. (1979). *Infrared Phys.* **19**, 599.

Ulrich, R., Renk, K. F., and Genzel, L. (1963). *IEEE Trans. Microwave Theory Tech.* **MTT-11**, 363.

van Nie, A. G. (1964). *Philips Tech. Rev.* **19**, 378–394.

Wang, W., Belford, R. L., Clarkson, R. B., Davis, P. H., Forrer, J., Nilges, M. J., Timken, M. D., Walczak, T., Thurnauer, M. C., Norris, J. R., Morris, A. L., and Zhang, Y. (1994). *Appl. Magn. Reson.* **6**, 195–215.

Weber, R. T., Disselhorst, J. A. J. M., Prevo, L. J., Schmidt, J., and Wenckebach, W. Th. (1989). *J. Magn. Reson.* **81**, 129–144.

Wong, M. (1989). Private communication.

Wylde, R. J. (1984). *IEEE Proc. H* **131**, 258–262.

Yu, P. K., and Cullen, A. L. (1982). *Proc. Roy. Soc. London Ser. A* **390**, 49–71.